nature reviews methods primers

https://doi.org/10.1038/s43586-025-00445-4

Primer

Check for updates

Operando ultraviolet–visible optical spectroelectrochemistry of surfaces

Benjamin Moss[1] ✉, Caiwu Liang[2], Andrew Carpenter[3], Lucas G. Verga[2], Soren Scott[4], Ryan J. R. Jones[1], Karthish Manthiram[1], Aron Walsh[2], Reshma R. Rao[1,5], Ifan E. L. Stephens[1] & James R. Durrant[6]

Abstract

Ultraviolet–visible spectroelectrochemistry (SEC) is a powerful and accessible operando technique for investigating redox-active interfaces such as electrodes. Its potential has not been fully realized owing to limitations in sensitivity, acquisition speed and analysis workflows. In this Primer, we describe how recent developments in optics, detection hardware and synchronization methods now allow for high-resolution, data-rich SEC measurements. We focus on practical strategies for building performant SEC set-ups, introduce a formalism based on differential coulometric attenuation for interpreting spectral changes and outline workflows for extracting redox stoichiometries, kinetics and coverage from complex data. Emphasizing process-sensitive over population-sensitive analysis, we show how this approach enables a clearer understanding of dynamic, disordered interfacial systems. Examples are provided from electrocatalysis, particularly the oxygen evolution reaction, but the principles described are broadly applicable. Throughout, we highlight pitfalls, assumptions and design choices to guide researchers looking to implement quantitative SEC in their own work.

Sections

[1]Department of Chemistry and Chemical Engineering, California Institute of Technology, Pasadena, CA, USA. [2]Department of Materials, Imperial College London, London, UK. [3]Andor Technology, Concord, MA, USA. [4]University of Copenhagen, Copenhagen, Denmark. [5]Grantham Institute — Climate Change and the Environment, Imperial College London, London, UK. [6]Department of Chemistry, Imperial College London, London, UK. ✉e-mail: benmoss@caltech.edu

Introduction

Materials that respond to voltage to convert or store energy are crucial for the transition to a low carbon economy. Technologies such as lithium-ion batteries[1], lithium-air batteries[2], electrolysers[3], electrosynthesis cells[4] and electrochemical alternatives to the Haber–Bosch process[5] all use complex, nanoscale solid–electrolyte interfaces to catalyse reactions, transport reactants and products and stabilize otherwise unstable materials. Functional nanoscale interfaces often form in situ, are highly sensitive to operational conditions and can evolve continually over time or with changes in operational parameters such as the applied potential or electrolyte composition[6]. Operando spectroscopies, which interrogate the nature of functional materials during operation, are therefore important tools to understand the nature of electrified nanoscale interfaces. Operando spectroscopic experiments that monitor the changes in the intensity of transmitted, scattered or emitted light that occur in response to applied potential can broadly be referred to under the term spectroelectrochemistry (SEC) and cover the entire electromagnetic spectrum, from X-ray absorption and emission measurements[7], visible-light Raman scattering[8], infrared absorbance[9] and terahertz spectroscopy[10].

SEC techniques measuring changes in the absorbance of electromagnetic radiation in the UV-to-visible (UV–Vis) range in response to steps or sweeps in applied potential are the most accessible as all that is required is a benchtop spectrophotometer, a cell and a potentiostat[11]. Redox changes occurring at electrified interfaces can produce very strong UV–Vis absorption changes and as a result, SEC can act as a highly sensitive probe of changes involving only very small numbers of states. Such changes can be used to quantify the degree of reduction or oxidation that is occurring at the interface, as well as distinguish different oxidation processes. This has been used to investigate the role of defect-induced low-valent metal sites in governing the efficiency of transition metal–oxide-based photoelectrochemical water splitting devices[12] and to track the growth of the depletion region induced by contact with an electrolyte in such devices[13]. Benchtop SEC has also been used to estimate the standard redox potentials of redox-active dopant sites in semiconductors[14], track oxidation changes in redox-active moieties in proteins[15,16] and determine the stability and speciation of the anionic states of polymers[17–19].

Because of its ability to quantify the extent of oxidation or reduction and distinguish different redox processes, SEC has also found utility in electrocatalysis. Here, the presence of multiple overlapping equilibria can result in surface redox dynamics that is challenging to assign. In such cases, kinetics becomes challenging to interpret as decays in current, optical signal and potential arise from contributions from multiple processes[20–28] (Fig. 1a).

Recent discussion in the field of electrocatalysis has highlighted the need for, and challenge of, using qualitative operando data to determine kinetics and thermodynamics of reactions. For example, electrocatalysts for the oxygen evolution reaction (OER) are often highly disordered hydrated metal oxides. The heterogeneous surfaces of these materials can in principle produce various surface bound states, some of which may participate as intermediates in a catalytic cycle and some not[29,30]. It has therefore been emphasized that the mere observation of a more oxidized state 'should not be considered sufficient to establish a mechanism without kinetic evidence of a TOF large enough to support the measured current'[31]. In contrast to single-crystal studies[32,33], in which the simplicity of surfaces greatly limits the number and nature of possible redox processes, the contribution of a putative intermediate to activity on a complex surface can only be determined by a measure of the rate of catalytic turnover. Of further importance is the absolute number of intermediates. The total rate, measured as current, is the product of the TOF of the rate-limiting intermediates and their surface density. Therefore, if an intermediate is determined to be involved in catalysis and highly reactive, it cannot be assumed to exist in sufficient density to support the measured current[20] as a less-reactive intermediate might exist at a much higher surface density and account for the majority of the measured current. A drive towards fast, data-rich and quantitative operando experimentation is therefore a natural focus of methodology development.

In this Primer, we outline the formal theory of SEC, the design of data-driven SEC instruments (with a focus on UV–Vis implementations) and best practices in experimental methods and interpretation. We show how these tools can be applied to extract the kinetics and thermodynamics of processes occurring on surfaces that are challenging to interrogate with other techniques. We use a synthetic data set to outline the analysis procedures in an interactive manner; by downloading the Python code from the GitHub archive for generating and analysing this data set, the reader can gain hands-on familiarity using with an ideal data set crafted to highlight the core concepts of the approach. We focus on electrocatalysis on surfaces and solid films, as this topic is less well covered in the literature, using the example of the OER on transition metal–oxide surfaces as this use case provides a strong motivating example for the application of SEC. Examples of oxidation reactions driven by positive polarization are provided (defined by standard oxidation potentials), although a similar rationale applies to reduction reactions. This Primer focuses on the SEC of solid interfaces rather than species in solution, in which diffusion transports products away from the interface — where they may react further — and limits the accessibility of reactants. These effects lead to unique considerations for experiment and cell design, and we refer readers to recent reviews[34–37] for a comprehensive discussion of solution-phase SEC.

Experimentation

In this section, we explain the advantage of moving to a dedicated SEC instrument. We then introduce the basic quantities measured in transmittance spectroscopy and provide a formulation of absorbance spectroscopy that directly contacts the electrochemical quantities that SEC seeks to differentiate.

Advantages of using a dedicated SEC instrument

A typical configuration for SEC is illustrated in Fig. 1b. Here, a spectroelectrochemical cell is placed in a benchtop UV–Vis spectrophotometer and potential is then independently applied in a three-electrode configuration to the cell and a spectrum measured. This process is then iterated to collect potential-resolved spectra. This process has the advantage of using widely available laboratory equipment, ensuring accessibility and a low startup cost. However, the accessibility of common SEC set-ups is counteracted by technical limitations as benchtop spectrophotometers are typically not designed for sensitivity, speed or synchronization with other devices. As this set-up is an ad hoc constellation of standalone devices that do not interact with one another, the user must manually and continually synchronize different parts of the experiment, for example, performing manual incrementation of the voltage and the collection of a spectrum. Furthermore, single spectra often require minutes to acquire as the single wavelength configurations commonly used in benchtop spectrophotometers spend only a small fraction of the total measurement time measuring photons of a given wavelength. These limitations mean that benchtop SEC set-ups

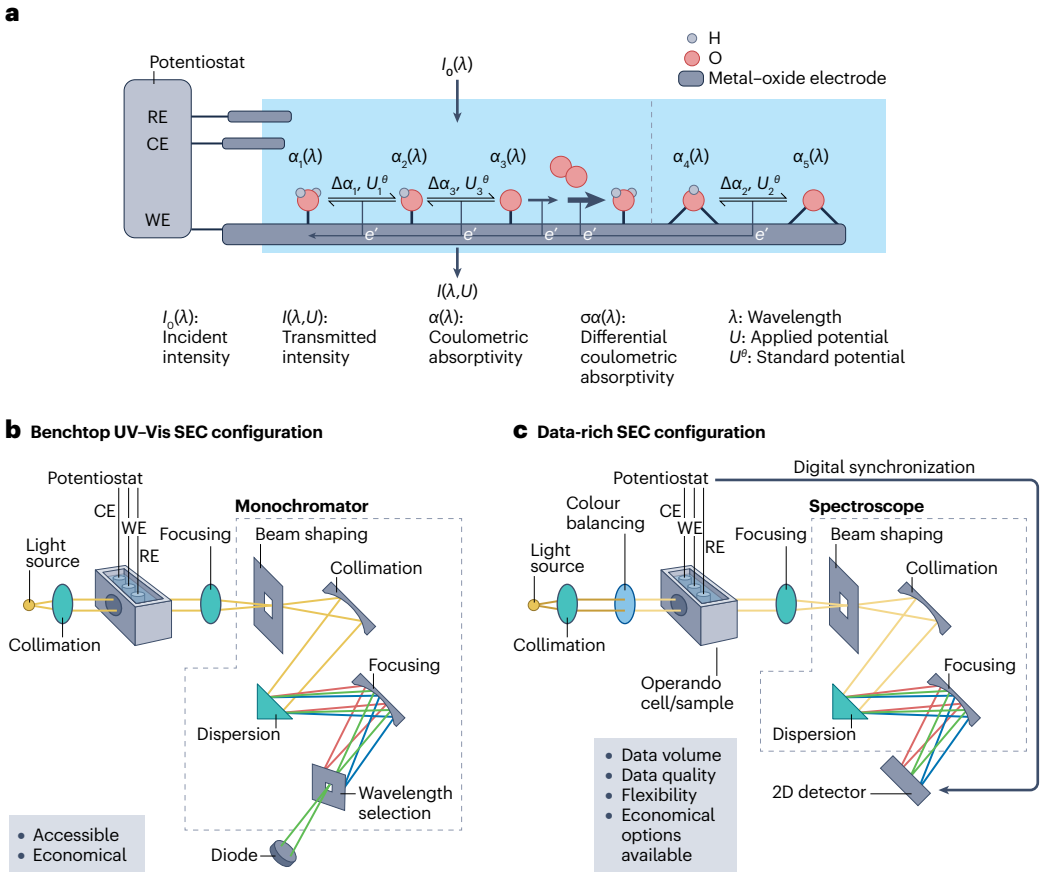

Fig. 1 | A simplified example of overlapping processes that may occur at an interface. a, The oxygen evolution reaction on a metal–oxide surface with two sites — a terminal oxygen site and a bridging site. The terminal site may be oxidized twice before forming a rate-limiting oxo intermediate, which rapidly reacts with water and turns over to form molecular oxygen. In this simple example, the bridging site may be oxidized once and is not directly involved in catalysis. This process occurs at a standard potential between the two oxidation processes of the terminal site and complicates analysis. The oxidation of sites changes the electronic structure of the interface, which may lead to a change in the intensity of transmitted light as the potential changes $I(\lambda, U)$. **b**, A standard UV–visible (UV–Vis) spectroelectrochemistry (SEC) configuration. Here, polychromatic light is collimated by a lens and passed through a cell holding, electrolyte and a transparent working electrode (WE). The cell also contains a reference electrode (RE) and a counter electrode (CE). Light is focused through a slit into a monochromator, where it is collimated by a parabolic mirror, dispersed by a reflection grating and then focused by another mirror. A single wavelength is selected by a slit and detected using a diode. **c**, A data-rich SEC configuration uses a multiplex detector to collect entire spectra simultaneously. The configuration is broadly similar but high-quality results are ensured by maximizing the output of the light source, filtering using a colour-balancing filter to ensure the spectrum used is as close to flat as possible and using a spectroscope that projects a spectrum onto a 2D detector.

are typically limited to qualitative analyses to determine the presence or absence of a given species in a window of applied potential[38] or in semiquantitative correlation analyses[24,28].

The advent of highly sensitive, low-cost, 2D sensors such as charge-coupled devices[39] (CCDs) and complementary metal–oxide–semiconductor[40] (CMOS) detectors, as well as improvements in synchronization hardware and software, allows for the detailed probing of the kinetics and thermodynamics of electrochemical interfaces. By projecting the entire spectrum onto a 2D camera, all wavelengths are integrated simultaneously, affording longer integration times per wavelength in comparison to single wavelength detectors while simultaneously affording subsecond spectral acquisition times (Fig. 1c). Economies of scale in 2D detector production[41] and the maturation of companies specializing in scientific grade 2D detectors such as Andor, Ocean Optics, StellarNet, Thorlabs, Tucsen photonics and Edmund Optics have created a diverse range of detectors capable of data-rich qualitative SEC, from portable spectrographs with small detector areas operating at room temperature (available at prices lower than a conventional UV–Vis spectrophotometer) to more advanced, large area, back-illuminated and deep-cooled CMOS and CCD cameras, affording superior sensitivity and time resolution. The diversity of detectors also facilitates a wide range of operating wavelengths, from the UV (~200 nm) to the near-infrared (NIR) (~1,800 nm). As a result, data-rich SEC techniques are now able to retain the accessibility of ad hoc approaches while providing data quality and volume needed for deep, quantitative analyses. The best balance of performance to operating range can be typically found in detectors optimized for the visible region, as detectors optimized to provide UV sensitivity commonly have reduced detection efficiencies and NIR-sensitive cameras typically cannot measure visible photons and have inherently lower

sensitivity and increased cooling requirements. Configurations using multiple detectors can provide maximum flexibility, but are beyond the scope of this Primer.

Despite the possibility of drastic improvements in data volume and quality, the majority of SEC research uses manual ad hoc experimental set-ups, single-wavelength configurations and qualitative analysis methods. The inability to collect fully quantitative data has naturally led to a lack of understanding in analysis. In this Primer, we focus on how fully quantitative SEC measurements can be generated through data-rich set-ups with improved detection capability and automated acquisition of potential resolved spectra.

Theoretical background. The simplest property associated with SEC is the absolute absorbance, which can be calculated from the incidence intensity $I_0(\lambda)$ and the transmitted intensity $I(\lambda, U)$:

$$A(\lambda, U) = -\log_{10}\frac{I(\lambda, U)}{I_0(\lambda)}.$$

Absolute absorbance is related to the density of each species in a system by the Beer–Lambert law:

$$A(\lambda, U) = l\sum_{\substack{\text{Species}\\ i}}^{N}\varepsilon_i(\lambda)C_i(U),$$

in which l is the path length in centimetres, and ε_i and C_i are the molar decadic extinction coefficient ($mol^{-1}\,dm^3\,cm^{-1}$, hereafter shortened to molar absorptivity) and concentration ($mol\,dm^{-3}$) of each species in the system, respectively.

SEC experiments are typically concerned only with states that change and react during the experiment, and not states that do not change (for example, an unchanging bulk absorbance contribution superimposed on a changing interfacial absorbance contribution). It is therefore most useful to consider absorbance relative to the absorbance measured from a starting potential (U_0):

$$\Delta A(\lambda, U) = A(\lambda, U) - A(\lambda, U_0) = -\log_{10}\frac{I(\lambda, U)}{I(\lambda, U_0)},$$

in which ΔA is the absorbance relative to a starting potential U_0; λ is the wavelength; $I(\lambda, U)$ is the intensity spectrum of the transmitted light (Fig. 1a) measured at a given potential and $I(\lambda, U_0)$ is the intensity spectrum measured at U_0.

It is worth emphasizing how ΔA is distinct from absolute absorbance. As shown in Supplementary Box 1, $A(\lambda, U)$ yields information about the total number of absorbing species in the system. In ΔA, however, the absolute absorbances of any species that do not change cancel. $\Delta A(\lambda, U)$ contains no information about the total numbers of species (indicated by $I(\lambda, U)$ versus $I_0(\lambda)$) and is only sensitive to relative changes resulting from the conversion of species. Note that $I_0(\lambda)$ should not be confused with $I(\lambda, U_0)$. Under circumstances in which conversion processes are monitored from start to completion, it might be possible to reconstruct absolute numbers of species given some assumptions of surface stoichiometry (see the 'Limitations and optimizations' section). Despite this, relative absorbance is a preferred quality of measurement as distinct processes can be clearly differentiated from one another, even in cases in which a complex background absorbance exists and the extinction spectra of the species undergoing interconversion strongly overlap (see Supplementary Box 1 for an example).

The form and units of the Beer–Lambert law are derived for the easy determination of absolute concentrations of species in solution, but for solid interfaces this formulation becomes cumbersome and ill-defined. The concept of path length (l) is complicated in cases in which the nanoscale interface of a material contributes to the relative absorbance and the micron-scale bulk of a thin film does not. Similarly, concentrations considered by the Beer–Lambert law are volumetric and might not be directly applicable to those on a surface. For SEC, it is therefore more convenient to consider the area density of species. As chemical reactions consume reactants and generate products in fixed stoichiometric ratios, we can therefore seek to study changes in area density, which can be related to a charge density. These concepts, which are outlined in more detail in Supplementary Box 1, suggest a form of the Beer–Lambert law better suited to SEC:

$$\Delta A(\lambda, U) = \sum_{\substack{\text{Process}\\ i}}^{N}\Delta\alpha_i(\lambda)Q_i(U),$$

in which $\Delta\alpha_i$ is the differential coulometric attenuation coefficient ($C^{-1}\,cm^2$, hereafter shortened to differential coulometric absorptivity), which describes the relative absorbance that would arise from driving an electrochemical reaction forward by the passage of 1 C cm^{-2} of charge around the external circuit. This change in absorbance arises owing to the difference in the differential coulometric absorptivities of the reactants and products (Fig. 1a). Q_i here is the partial charge related to a given redox process (i), with unit C cm^{-2}. We recommend using this formulation and will use it hereafter.

SEC workflow for understanding redox dynamics and kinetics

There exist as many possible SEC experiments as voltametric techniques. In this Primer, we focus on UV–Vis SEC, which provides an accessible and versatile platform for probing redox dynamics. Within this framework, we have found utility in a workflow coupling UV–Vis spectroscopy to three voltametric profiles, which we introduce in detail in the following sections.

We begin with cyclic voltammetry SEC (CV-SEC), which forms the core of this workflow as it proves quantitative dynamics of the redox processes that occur on surfaces, revealing the potential windows in which distinct processes dominate and providing access to mechanistic descriptors such as intermediate binding energies and turnover frequencies (TOFs) normalized by the density of potential-dependent species. We then discuss square-wave voltammetry SEC (SW-SEC), which is used to calibrate absorbance against charge and ensures that charge transfer to the catalyst surface is not rate-limiting. Finally, potential decay-SEC (PD-SEC) confirms the reactivity of the species identified as critical to the catalytic cycle. Only by combining these techniques can the full potential of any be achieved; as without the detailed dynamics provided by CV-SEC, SEC potentials for the other two techniques are effectively chosen blindly. Similarly, without SW-SEC and PD-SEC, CV-SEC cannot be calibrated to give partial charge dynamics or be confidently interpreted to give binding energy or TOF.

All workflows described subsequently are illustrated using synthetic data, which can be reproduced by running the main.py script and subsequent plotting scripts available in our GitHub archive.

Cyclic voltammetry spectroelectrochemistry. During a potential ramp, increasing potential drives the oxidation of species at the surface of an electrocatalyst (Fig. 1a). Each of these redox processes has its own standard potential. Where the applied potential exceeds the

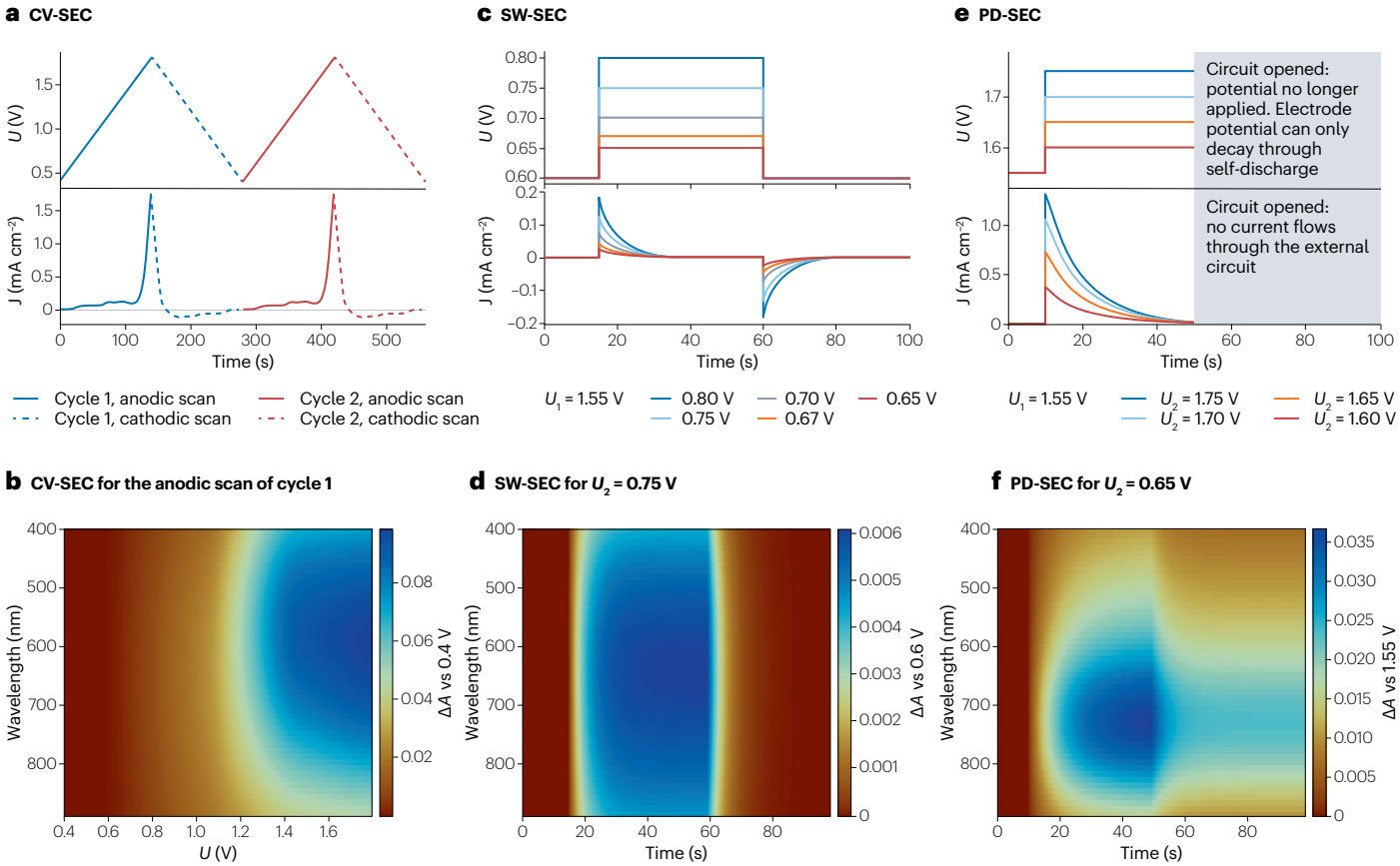

Fig. 2 | Typical spectroelectrochemistry experiments and example data. **a**, Potential–time (top) and current–time (bottom) traces of a cyclic voltammetry spectroelectrochemistry (CV-SEC) experiment. **b**, SEC data of a single scan of the experiment, showing complex evolution of differential absorbances with potential (corrected by voltage drop arising from solution resistance, iR). **c**, Potential–time (top) and current–time (bottom) traces for a series of square-wave SEC (SW-SEC) experiments starting at a common lower potential and with increasing upper potentials. **d**, SW-SEC spectra for a single experiment showing the spectral dynamics that evolves and decays during an experiment. **e**, Potential–time (top) and current–time (bottom) traces for a series of potential decay-SEC (PD-SEC) experiments starting at a common lower potential and with increasing upper potentials. **f**, PD-SEC data for a single experiment; here, the circuit is opened and spectra may only decay through self-discharge processes. All data shown in this figure are synthetic and obtained by simulating absorptivity spectra with mixtures of broadened gaussians (details can be found in our GitHub archive). For CV-SEC, the evolution of the spectra is governed by the equations provided in this Primer. For simplicity, kinetics is simulated with either exponential (SW-SEC) or power-law (PD-SEC) functions.

standard potential, an oxidation 'wave' is observed because, unlike solution electrochemistry, a limited amount of material is available to oxidize, leading to self-limiting redox processes. Ideally, the standard potentials of these redox processes are far apart enough to allow the current 'waves' for each process to be discerned, assigned and analysed (see the 'Results' section). This is often the case for single-crystal facet electrodes. However, in polycrystalline electrodes, transitions can be broadened by a multitude of factors (see the 'Results' section) and might overlap in potential. In this case, correlating spectral evolution with charge passed allows overlapping redox processes to be distinguished and quantified.

In CV-SEC, spectra are measured continuously as cyclic voltammetry is performed (we refer readers inexperienced in cyclic voltammetry to refs. 42,43 for an introduction to this technique). Here, the potential, U, is applied in a three-electrode configuration, compensated against solution resistance (see refs. 44,45 for a detailed discussion of iR compensation) and increased linearly with time at a scan rate of ν (V s^{-1}) from a lower vertex potential to an upper vertex potential (that is, an anodic scan). After this point, the scan direction is reversed ($-\nu$) and the potential is driven back towards the lower vertex potential (in a cathodic scan) to complete a cycle that can then be repeated (Fig. 2a, top). During this measurement, the current density J (A cm^{-2}) that is drawn in response to the change in potential is recorded (Fig. 2a, bottom). As electrochemical systems exhibit capacitance (units F or, more usefully, $\frac{C}{V}$), the measured current is sensitive to both the potential and the scan rate.

To collect CV-SEC, spectra must be collected during a CV measurement, requiring the two to have a common starting time. Spectral acquisition is most easily synchronized by sending a voltage pulse known as a trigger or transistor–transistor logic pulse from the potentiostat to the detector at the start of the experiment, with the camera measuring continually at the fastest possible acquisition time to produce a sufficient signal until the experiment ends. We typically perform voltammetry at scan rates of 1–10 mV s^{-1} with an exposure time of ~10 ms to enable

10–100 exposures to be averaged to produce a data set with 1 spectrum per millivolt. Maximizing the intensity of light such that the number of counts per exposure is close to the upper end of the dynamic range of the detector is crucial for the success of this strategy.

Practically speaking, synchronization can be achieved by coupling transistor–transistor logic trigger pulses with standard instrument control software or programmatic synchronization using an automated programming interface with a coding language such as Python, C or LabVIEW. As the potentiostat and the camera have a common starting time or known time offset, a spectrum measured at a given time can be interpolated to a given potential. An alternative approach is to use an automated programming interface to develop a loop incrementing the potential and then recording both the current and the spectrum. The latter removes the need to interpolate potentials with times, although it reduces the acquisition rate. In both cases, the relative absorbance spectrum (Supplementary Box 1) for a particular cycle c and scan s (for example, cycle 1, anodic scan) is shown in Fig. 2b and is calculated by:

$$\Delta A(\lambda, U, c, s) = A(\lambda, U, c, s) - A(\lambda, U_0, c, s) = -\log_{10}\frac{I(\lambda, U, c, s)}{I(\lambda, U_0, c, s)}.$$

It is worth emphasizing that the evolution of the spectra will be strongly cycle-dependent if the surface changes irreversibly with time during the CV and strongly scan-direction-dependent if there is irreversibility or hysteresis between oxidation in the forward scan and reduction during the reverse scan. In a reversible system, the scan number can be ignored and a single scan direction chosen (for example, anodic scans only). Initially, however, both should be examined to determine whether the cathodic scan simply constitutes the reversal of the anodic scan, with some degree of hysteresis, or whether irreversible changes occur upon cycling.

Square-wave voltammetry-spectroelectrochemistry. A crucial aspect in understanding an electroactive material is understanding the kinetics of charging and discharging associated with a given surface redox process. Charge transport to the interface in a material that is too insulating or thick might be so slow as to be rate-limiting. Furthermore, as redox processes might influence the conductivity and charge transport of films[46], it is useful to assay the charge transport kinetics in a process-specific manner. Another challenge is determining the value of $\Delta\alpha_i$ at the wavelength where absorbance is maximal ($\Delta\alpha_i(\lambda_{peak})$, see the 'Results' and 'Applications' sections for more details).

Square-wave voltammetry SEC can be used to accomplish the aims mentioned earlier. A window of potential should be chosen where only one process dominates (see the 'Results' section for details); within this window, a square wave is applied, abruptly changing the baseline potential U_0, t_0 to an upper potential U_1 at time t_1 and back to U_0 at t_2 (Fig. 2c, top panel). In response to the potential step, the electrode exhibits a charging transient, which is recorded by the potentiostat (Fig. 2c, bottom panel). This transient decays as the electrode reaches a new position of equilibrium. The optical detector is triggered at the start of the experiment and records throughout. The relative absorbance (Fig. 2d) as a function of time is calculated as:

$$\Delta A(\lambda, t) = -\log_{10}\frac{I(\lambda, t)}{I(\lambda, t_0)}.$$

To understand changing dynamics across the potential window, and to extract the magnitude of $\Delta\alpha_i(\lambda_{peak})$, this experiment is typically performed over a series of U_1 values as in Fig. 2c. This leads to larger current transients as more charge must be passed for the system to reach quasi-equilibrium.

Potential decay-spectroelectrochemistry. Since early work by Conway in the 1950s, it has been recognized that the reactivity of species accumulated through charging an electrode can be monitored by the decay in electrode potential under conditions in which no charge can cross the external circuit[47]. After a fast drop related to solution resistance[48], the electrode potential can only change through coupled reduction or oxidation reactions that enable the electrode to discharge and therefore decay towards a potential that minimizes the energy of the system. In the Nernst equation, the electrode potential is logarithmically related to the reaction quotient (Supplementary Box 1) — the ratio of product to reactant activity raised to their stoichiometric coefficients. However, this decay in potential is ambiguous in situations in which multiple intermediates coexist and decay simultaneously.

In PD-SEC, the decay of relative absorbance under open circuit is a direct probe of the interconversion of states occurring as a result of reaction. A constant potential is applied for a time in a similar manner to SW-SEC. However, instead of returning to the starting potential at t_2, the circuit is opened, preventing the passage of charge. Total current is zero and the potential drifts as a result of balanced anodic and cathodic processes occurring at the surface (Fig. 2e). The electrode potential with respect to the reference electrode can be measured if desired, but is not necessary for analysis. The detector is again triggered at the start of the measurement, with $\Delta A(\lambda, t)$ calculated identically to SW-SEC, and records both the generation of intermediates and the self-discharge reactions (if any) that the products of a redox process can undergo after they are generated (Fig. 2f).

As with SW-SEC, it is simplest to choose values of U_0 and U_1 that correspond to a potential window where only one redox process is occurring and thus correspond to the generation of increasing amounts of only one product that might affect the decay rate. The technique can also be useful in distinguishing quick-decaying reactive species from slow-decaying, unreactive species, in which it can be proven that the products of multiple processes coexist at a given potential.

Choice of experimental components

Data-rich SEC systems are not currently available to purchase and must typically be assembled. All SEC set-ups broadly speaking follow the schematic shown in Fig. 1b, which indicates how entire spectra are projected onto the detector. Practically speaking, turnkey spectrographs for the dispersal of spectra and collection of spectra are readily available and compatible with detectors of the same brand. The major components of any set-up are detailed subsequently.

Light source. The relative absorbance in an SEC experiment can be written as:

$$\Delta A(\lambda, U) = -\log_{10}\left(1 - \frac{\Delta I(\lambda, U) + \mathrm{err}(\lambda)}{I_0(\lambda)}\right),$$

where ΔI is the change in the intensity that occurs because of the changing absorbance of the sample and $\mathrm{err}(\lambda)$ is a noise function that depends on the light source, the detector and the wavelength. The function $\log(x)$ behaves asymptotically in the region where x is close to 0. In this region, small fluctuations in x will produce a large fluctuation in $\log(x)$. Ideally, therefore, the term $\Delta I(\lambda, U) + \mathrm{err}(\lambda)$ should always be small in comparison to the intensity of light on the detector ($I_0(\lambda)$) to avoid the

situation in which $1 - \frac{\Delta I(\lambda, U) + \mathrm{err}(\lambda)}{I_0(\lambda)}$ is close to 0, as here, a small random effect of $\mathrm{err}(\lambda)$ will induce asymptotic fluctuations in ΔA. This situation can be unavoidable in optical set-ups where the light source is weak, or where very little light reaches the detector.

To avoid the problem mentioned earlier, a light source that is as stable as possible and intense across the wavelength range being studied must be used. Good choices for the 400–900 nm range are stabilized, low-noise, W-halogen lamps as they meet these criteria: low cost and a small physical footprint (the authors have used Thorlabs SLS201L and Bentham WLS100). These sources are also capable of emitting into the NIR, enabling the use of a single source for configurations with both visible and NIR detectors. Deuterium sources can be used for measurements in the UV region, although the sharp, intense peaks in these spectra must be carefully filtered out if high intensities are to be used without inducing artefacts in the spectra associated with detector saturation (Supplementary Table 1). An array of UV-light-emitting diodes (LEDs) combined using a fibre-optic patch cable can also be used. In this case, LEDs must be effectively cooled and it is therefore recommended to buy LEDs equipped with heat sinks or to invest effort in designing effective cooling solutions.

For the sake of simplicity, the optical configurations discussed in this Primer do not use a reference beam to measure fluctuations in the lamp output intensity (I_0). Gas discharge lamps such as Xe arc lamps are a less-suitable choice for set-ups not using a reference beam as, despite their intense output, the flickering of the arc of plasma between the two electrodes of the lamp produces large changes in intensity that can overwhelm $\Delta I(\lambda, U)$. If arc lamps are desired, the reader is advised to pay close attention to stability and design configurations to minimize variation from flicker.

Collimation, colour balancing and light guides. Light sources contain a slit, aperture or fibre-optic collector to select light travelling out from the light source in the direction of interest. In the ideal situation, this light should act as point source (a source in the the shape of a sphere with an infinitesimally small radius). Emitted light diverges with distance, leading to an intensity that decays with the square of distance from the source. For a sufficient number of photons to pass through the sample and to the detector, light must be collimated using a lens. A lens of focal distance f will collimate a point source when placed f mm from the source. More light can be collected using lenses with smaller focal lengths, although smaller focal length lenses tend to also have smaller diameters (D). Thus, a pertinent number for the collection ability of the lens is the numerical aperture N, which can be expressed as:

$$N = \frac{f}{D}.$$

For situations in which maximal collection efficiency is critical, it might be pertinent to choose optics that maximize collection. However, for most contexts, footprint and price point are also relevant considerations. About 6 cm focal length planoconvex lenses with a diameter of 2 in. are an economical and performant choice (the authors have used Thorlabs LA1401-AB, although any lens from a trusted supplier will work). Choosing achromatic lenses — those corrected for small changes in focal point that occur with different wavelengths — is an option at a higher price point and will produce slightly better intensities and focusing characteristics. It is also worth noting that many suppliers provide light sources with collimators as a convenient add-on. Lenses can be mounted on to movable optical posts and post holders, and alignment eased with optical rails or optical cage systems.

Both W-halogen lamps and LEDs exhibit an emission spectrum with a strong peak. Thus, detectors might become saturated at the peak emission wavelength and register very low intensities at wavelengths far from this peak. This problem can be mitigated by using a colour-balancing filter to attenuate light at the peak wavelength and produce a flatter emission spectrum. The authors use Thorlabs FGT200 filters in conjunction with a range of W-halogen sources for this purpose. Although maximizing light intensity is helpful to obtain a flat spectrum which is as intense as possible, too much light will eventually saturate any detector regardless of whether colour-balancing filters are used. In this case, using neutral density filters or moving a lens out of the focal plane can reduce intensity evenly across wavelengths.

A light guide might be required if there is a need to direct light in complex, nonlinear, 3D paths. Two types of light guides are available: liquid light guides, which typically have larger core diameters (2–10 mm), and fibre optics, which typically have smaller core diameters (0.1–1 mm). Although fibre optics collect less light than liquid light guides, they have the advantage of having a standardized optical coupling. Low-cost modular spectrometers typically come with fibre optics and if used should be mounted at the point of maximum intensity of the focused beam. In all cases, care should be taken to ensure that the light guide chosen transmits in the desired wavelength region by selecting a guide with an appropriate wavelength operating range. Furthermore, note that light guides work on the principle of total internal reflection and should not be overly bent.

Spectroelectrochemical cells. Once collimated, light must pass through the sample cell. The design and materials used for this cell will depend on the function of the material being studied and the wavelength range used, as well as other factors such as the need for increased pressure, flow or other conditions. For electrocatalysis, the authors have found that a simple, single-chamber cell with a mount to keep the working, reference and counter electrodes from touching is fairly simple to machine and versatile (see schematics in the Supplementary Data). Polyether ether ketone is a suitable material for the cell body and any parts that might come into contact with electrolyte as it is resistant to strong acids, bases and organic solvents, and can be soaked in aqua regia to remove trace metal contamination. Another similarly viable material is polytetrafluoroethylene. The optical window of this cell is quartz to enable studies using UV light, although a glass window will work equally well if only the visible region is of interest. Ultimately, the material chosen will depend on the conditions of the experiment. For example, a cell composed entirely of glass might be inappropriate for experiments in strongly basic media over long times and for experiments susceptible to contamination by trace metals released from the glass as it etches under these conditions (see ref. 45 for a detailed account of standard electrochemical practices that apply equally to SEC). For materials such as polyether ether ketone, machining is the only way to produce a cell, which leads to considerable expense and a slower development cycle. Stereolithographic 3D printing enables cells to be rapidly prototyped and can produce cheap and chemically resistant cells[49], and the authors have had excellent results using high-end printers (Form 4) and tolerable results with budget printers (Elegoo Saturn 4 Ultra). We encourage the reader to check the reported chemical compatibility and to thoroughly test the chemical compatibility of resins before committing to long-term cell use. Fused deposition modelling printers (also known filament printers) should be avoided as the gaps between filaments can trap electrolytes, leading to longevity and contamination issues[49].

Sample preparation. For measurement of transmitted light, all samples must be deposited on an optically transparent substrate. Glass coated with transparent conducting oxides such as fluorine-doped tin oxide is an excellent choice for oxidative and mildly reducing potentials on the reversible hydrogen electrode scale, but is unsuitable for strongly reducing conditions[50]. The reader is referred to ref. 50 for a detailed discussion of substrate suitability. Samples can be deposited by a range of methods such as drop casting[18], sputtering[26], electrodeposition[23] and hydrothermal synthesis[20]. Samples should not be strongly insulating or overly thick (greater than ~1 µm) to avoid creating highly resistive paths to the surface[51]. Samples should also ideally be single phase as the coexistence of multiple phases corresponding to different materials can produce highly complex and congested spectra that take considerable time to unravel.

Dispersion of spectra. Depending on the price point, turnkey spectrographs can be fibre-coupled or require the user to focus light into a spectroscope. In the former case, light must be focused down into the aperture of a receiving fibre optic, which can be achieved with the same type of lens used to collimate the beam. Here, the key consideration is to ensure that the fibre-optic aperture is well aligned with the beam. At higher budgets, cage systems can be used to guarantee alignment. However, a user can be just as successful with manual alignment, placing the fibre optic and focusing lens on posts mounted on an optical rail and then adjusting the distances and angles to maximize the detected intensity. For higher price points, the beam is directly coupled to an entrance slit of the spectroscope. To match the acceptance cone of the spectroscope, focusing optics with an appropriate *f*-number are required ($f\# = \frac{f}{D}$, in which f is the focal length of the lens and D, in this case, is the diameter of the collimated beam)[52]. It is recommended that the reader checks the *f*-number of the spectroscope and chooses optics accordingly. With large area 2D detectors, it may be advantageous to adjust the distance of the focusing lens away from the distance where throughput is maximized to ensure that light is projected evenly across the height of the detector and not simply in the centre; this can be done by moving the focusing lens closer to the spectroscope.

The wavelength resolution of a spectroscope is fixed by its internal optics and number of lines per millimetre of the reflective grating used to disperse the spectrum. Users should be aware that there is a trade-off between wavelength resolution and the bandwidth — the wavelength range that can be captured with one image. Larger bandwidths allow the user to study a wider range of wavelengths, although higher wavelength resolutions allow narrower peaks to be resolved. A balance should be prioritized in the study of solid interfaces as the bandwidth must be sufficient to resolve broad spectral signatures but multiple wavelengths can be averaged together by downsampling to improve resolution and signal-to-noise ratios. For example, if three wavelengths per nanometre are recorded, these can be downsampled to 1 nm resolution, increasing averages by a factor of three.

Detection of spectra. The core of a data-rich SEC set-up is the detector. The choice of the detector will depend on price point and anticipated usage, light intensity and acquisition time. The principles of operation, use cases and pitfalls of the two most common camera types (CCD and CMOS) are illustrated in detail in Supplementary Box 2.

CCD cameras have been the key camera technology for spectroscopy but are generally not optimal for high-speed, high-light-intensity acquisitions owing to their use of a common readout node. The analogue-to-digital conversion (ADC) unit on CCDs is typically 16-bit, implying that the upper end of the dynamic range is 2^{16} (65,536) counts. Under bright conditions, pixels are not designed to hold more photoelectrons than this value and overflow once saturated, leading to bloom artefacts (Supplementary Box 2). Additionally, resolving weak responses next to strong responses can be limited by the 16-bit dynamic range. Spectra are typically recorded by CCD cameras in full vertical binning mode, in which pixels in each column are summed into the shift register pixel before horizontal readout. This speeds up spectral acquisitions over full-frame imaging, but comes at the cost of dynamic range as there is a 16-bit effective upper limit of the sum of pixels in a column. CCD users are strongly advised to check images for saturation to avoid inadvertently recording a bloom artefact.

Scientific CMOS (sCMOS) technology is newer than CCDs and historically has required additional linearity and aberration corrections to be fully quantitative (discriminating CMOS imaging devices from scientifically quantitative sCMOS devices). These corrections were first implemented around 2008 (ref. 53), although their adoption in spectroscopy applications has been much slower than imaging experiments. Unlike CCD cameras which convert electrons to voltage on the shift register, the pixel-level signal conversion in sCMOS is advantageous for SEC, as although the dynamic range of an individual pixel remains 16-bit, total signal sizes are recorded after ADC, with pixel readout values being summed on a 32-bit ADC register. As such, the upper limit of a column's dynamic range is the pixel dynamic range (65,536) multiplied by the number of pixels in a column. This advantage can be maximized by choosing larger area detectors; with several thousands of pixels per column, the upper limit of dynamic range for a single acquisition can be as high as 10^8 counts. In this optimal regime, the relative contribution of noise from the detector is minimized and the primary source of noise arises from oscillations in the intensity of the light source. In its fastest acquisition mode — rolling shutter mode — the CMOS camera reads middle rows first and rows towards the top and bottom last, which can lead to 'rolling shutter imaging artefacts' (Supplementary Box 2). This is typically not an issue for spectroscopy, in which vertical columns of the detector are averaged together, although it is worth noting that a spectrum results from the average of many individual spectra recorded at slightly different times; this is a potential limitation in instances in which users aim to resolve fast phenomena.

Data collection and software. Collection of data requires the synchronization of the detector and the potentiostat. The simplest approach for synchronization is to acquire data from the two instruments separately and use timestamps stored in the data files to calculate the offset and to align them in time. Combination and alignment of the data in processing can then be performed using software packages such as ixdat. This approach only works when the data output includes timestamps that are sufficiently precise to align accurately with.

The next-simplest approach for synchronization is to use bundled software (such as Metrohm's NOVA, Gamry's Framework and Biologic's EC-Lab) to send a trigger from the potentiostat and to instigate a measurement from the camera software (for example, Andor's Solis and Ocean Optics' Ocean View). The potentiostat software will read as normal and data can be manually saved at the end of measurement into any common text format. A set series of acquisitions (kinetic series) is initialized on the camera by the trigger. The number of acquisitions and the exposure time should be set such that their product will be of a similar time to the total time required to perform the measurement. For example, a cyclic voltammogram with two vertexes (U_1 and U_2) will take $2\frac{n(U_2 - U_1)}{\nu}$ seconds, in which n is the number of cycles (if the cyclic

voltammetry process starts and ends at U_1). The kinetic series will acquire for approximately mt_{exp} seconds (some time is lost reading data out between acquisitions), in which m is the number of acquisitions in the series and t_{exp} is the exposure time. Assuming optimal circumstances in which the number of counts measured is near to (but not over) the upper limit of the camera's dynamic range at the minimum exposure time for the camera, one should choose the minimum exposure time available. Larger exposure times should only be used if the signal is close to the lower end of the dynamic range. It is prudent to choose m such that the camera measures for slightly longer than the window for acquiring the cycling voltammogram, as these later times can be removed in post-processing.

$U(t)$ data from a cyclic voltammogram can be used to generate a function that interpolates a time measured in the spectra to potential (for example, fitting the $U(t)$ in the CV data to a triangle wavefunction). This can be done in any data analysis software. For an example of how the authors implement this, see the Sawtooth 2 function in the SEC_class_2.py file in the GitHub archive that accompanies this Primer. Linear interpolation can also be used. After interpolation, potentials can be associated with the spectrum from each acquisition, enabling the spectral data to be broken down into spectral data for a given scan and cycle. Note that it is important that these potentials are iR-corrected and not raw applied potentials. At this point, relative absorbance can be calculated. Custom-designed Python or LabVIEW control software can automate experiment and streamline experiment and analysis, which we have used for generating our example data. Unfortunately, to date no operating software is compatible with all common brands of potentiostat and spectroscope; the choice of synchronizing instrument software, using/modifying existing custom software or building your own will depend on frequency of usage and the components that are purchased. The authors are aware of this challenge, and standardized operating and analysis software is under active development.

Results

In this section, we outline analysis procedures for interpreting and extracting useful information from related CV-SEC, SW-SEC and PD-SEC data. We show how partial charges and currents for redox processes can be extracted from CV-SEC, differential coulometric attenuation coefficients and charge/discharge kinetics can be extracted from SW-SEC, and finally how intrinsic reactivity can be quantified using PD-SEC.

CV-SEC

After calculating the relative absorbance of a scan, the first step is to check the stability of the process dynamics. If a surface corrodes or becomes passivated, a process that proceeds but cannot be reversed will be measured. An irreversible process that does not produce a signal in the UV–Vis region will still likely affect the density and energetics of interfacial redox processes. Stable process dynamics is, therefore, characteristic of interfacial stability on the timescale of the CV experiment. This can be tested by taking the CV-SEC spectra from adjacent cycles (Fig. 3a) and subtracting them:

$$\text{Irreversible}\Delta A = \Delta A(\lambda, U, c, s) - \Delta A(\lambda, U, c-1, s).$$

The stability of process dynamics can also be measured across large time intervals, for example, between the first and last cycles.

An example of a result showing stable process dynamics is Fig. 3b, in which the spectra shown in Fig. 3a are subtracted. The data should be within the noise bound of the system, which can be measured by performing an experiment on a bare fluorine-doped tin oxide substrate that gives no change in absorbance. If strong irreversibility (>5% of measured signal) is measured, the sample might be undergoing degradation or irreversible bulk phase transformation, in which case the following analysis should not be performed. In cases of passivation, overlayer growth or self-limiting process changes in surface structure. To distinguish self-limiting processes from continuous corrosion, cycling should proceed until stable process dynamics is observed; if stability is not obtained, the following analyses will not be valid. If stability is obtained, the following analysis is valid. However, it should not be assumed that the measured surface and the native surface are the same.

Returning to the equation relating partial charge and relative absorbance:

$$\Delta A(\lambda, U) = \sum_{\substack{\text{Process} \\ i}}^{N} \Delta\alpha_i(\lambda) Q_i(U).$$

If a potential window $[U', U' - \delta U]$ exists in which one redox process is predominant, the difference of two ΔA spectra in this window should be dominated by spectra reporting on that process:

$$\begin{aligned}\Delta A(\lambda, U') - \Delta A(\lambda, U' - \delta U) &\approx \Delta\alpha_i(\lambda)(Q_i(U') - \Delta\alpha_i(\lambda) Q_i(U' - \delta U)) \\ &\approx \Delta\alpha_i(\lambda)\delta Q_i(U'),\end{aligned}$$

in which $\delta Q_i(U') = Q_i(U') - Q_i(U' - \delta U)$. For context, the authors use U–δU intervals of 1–20 mV, depending on the magnitude of the changes observed. The smallest interval that generally shows a change that is sufficiently above the noise should be chosen. For example, a user may start with a 20 mV interval but subsequently find that changes can be resolved at 5 mV, enabling a more fine-grained analysis. Normalizing spectra in this region produces an identical result as the spectra are simply $\Delta\alpha_i(\lambda)$ scaled by a constant. The result is the normalized coulometric attenuation coefficient for the process, $\overline{\Delta\alpha_i}$:

$$\frac{\Delta\alpha_i(\lambda)\delta Q_i(U')}{\Delta\alpha_i(\lambda_{peak})\delta Q_i(U')} = \frac{\Delta\alpha_i(\lambda)}{\Delta\alpha_i(\lambda_{peak})} = \overline{\Delta\alpha_i}(\lambda).$$

Thus, by searching for regions in which the normalized spectra arising from $\Delta A(\lambda, U') - \Delta A(\lambda, U' - \delta)$ become convergent, one can ascertain $\overline{\Delta\alpha_i}(\lambda)$. Regions in which successive spectra diverge from one another are regions where the mixed processes are happening and changing in proportion to one another with increasing potential. An example showing the evolution of normalized difference spectra is shown in Fig. 3c. Convergent spectra (corresponding to $\overline{\Delta\alpha_i}$) are picked out and plotted in the bottom panel. We encourage the reader to interact with these data, available on GitHub, to satisfy themselves that the spectra chosen are indeed convergent.

Using these values, one can fit $\Delta A(\lambda, U)$ to a linear combination of $\overline{\Delta\alpha_i}(\lambda)$ values:

$$\Delta A(\lambda, U) = \sum_{\substack{\text{Process} \\ i}}^{N} \overline{\Delta\alpha_i}(\lambda)\beta_i(U),$$

in which the fitting coefficient is given by $\beta_i(U) = \Delta\alpha_i(\lambda_{peak})Q_i(U)$. The fitted process dynamics (Fig. 3c) is therefore proportional to the partial charge passed and provides information about the potential windows in which processes occur, as well as the degree of completion of each

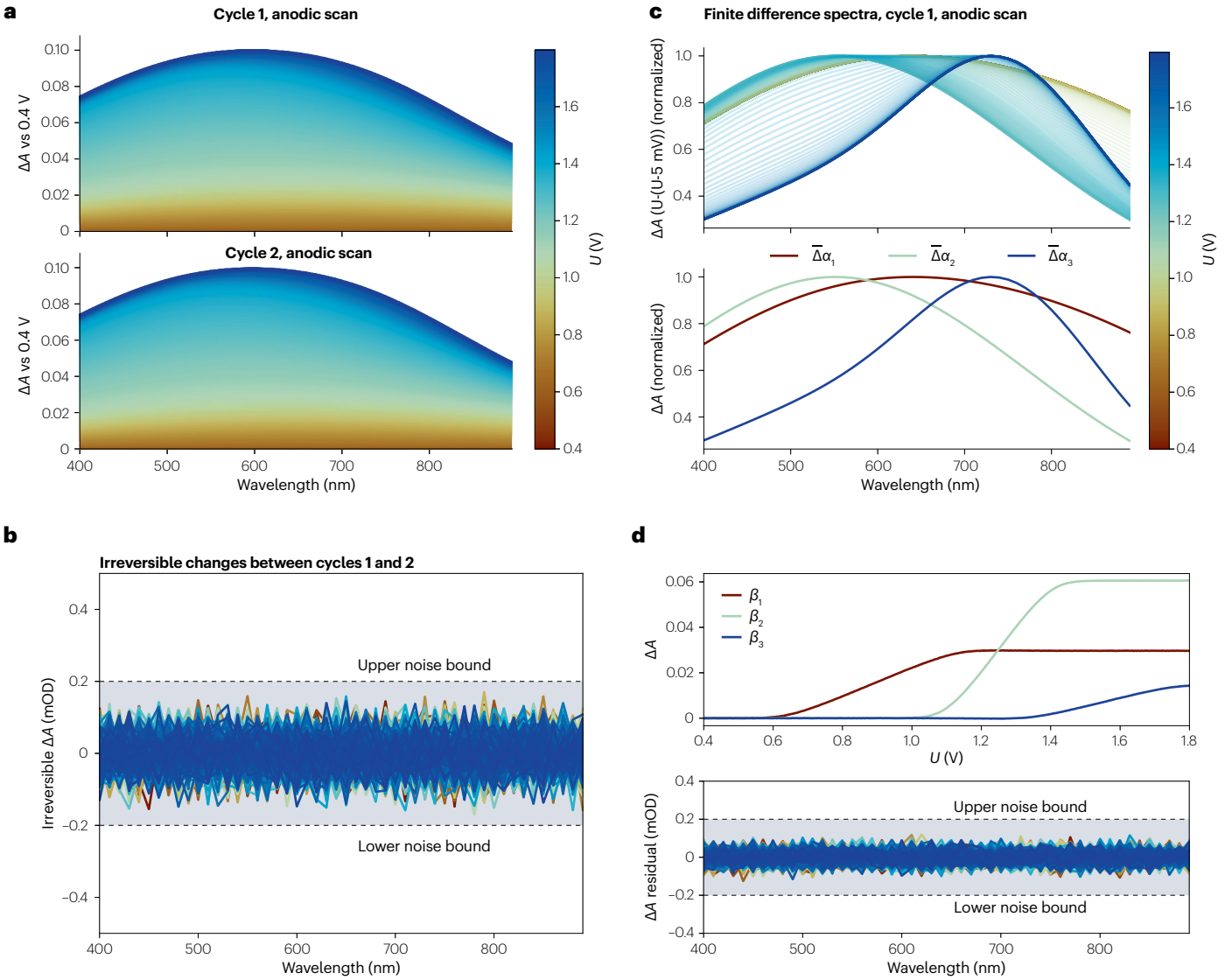

Fig. 3 | Example analysis of synthetic cyclic voltammetry-spectroelectrochemistry data. a, Cyclic voltammetry-spectroelectrochemistry data showing relative absorbance plots for the anodic (positive) scan of two subsequent cycles. **b**, The irreversible change in absorbance from subtracting the spectra in part **a**. **c**, Normalized differential absorbance spectra (top), with convergent regions (yellow, teal and dark blue) indicating normalized differential attenuation spectra (bottom). **d**, Top: fitting coefficients (β_i) from a linear fitting of data in part **a** to the normalized attenuation spectra in part **b**. Bottom: residuals of the fit, obtained by subtracting the measured spectrum from the reconstructed spectrum. mOD, milli-optical density. All data shown in this figure are synthetic and obtained by simulating absorptivity spectra with mixtures of broadened gaussians (details can be found in our GitHub archive).

reaction ($\alpha_i = \beta_i/\max(\beta_i)$). As β_i and partial charge Q_i are proportional to one another, the degree of completion can also be written as $\sigma_i = Q_i/\max(Q_i)$. For a process that is limited to the surface, where the product is not consumed by a subsequent process, the degree of completion is equivalent to the surface coverage (θ_i). This equivalency rests on the assumption that for a simple single-electron interconversion process ($A \rightarrow B + e^-$) that is observed from start to finish, the number of moles of A converted (or the number of electrons passed) divided by the total number of moles of A available (equivalent to the total number of moles of A converted once the process has completed) gives θ ($\theta = \sigma$). In cases in which B is subsequently consumed by another process, the equivalency of θ and σ fails. Thus, this assumption cannot be made without supporting measurements or domain knowledge (see the 'Limitations and optimizations' section). The exception to this rule is if the process in question is the last one observed in the potential window, as here, there are thus no subsequent processes to consume it. In real experimental data, there are various reasons why artefacts, low signal or high noise might occur. This can make picking out convergent regions, as shown in Fig. 3c, more challenging. In this case, it is especially important to confirm the choice of $\overline{\Delta\alpha_i}(\lambda)$ by plotting the residuals (Fig. 3d, top panel) of the fit ($\Delta A_{\text{resid}}(\lambda, U) = \Delta A_{\text{measured}}(\lambda, U) - \Delta A_{\text{fit}}(\lambda, U)$). The residuals should ideally be close to the noise of the measurement (Fig. 3d, bottom panel).

SW-SEC

The fitted data in Fig. 3d (top) provides information about the process dynamics of the system, as it indicates the relative amounts by which the electrochemical processes that interconvert species at the interface are proceeding. Using this plot, windows of potential in which each process is predominant can be extracted. In the example shown in Fig. 3d (top), process 1 predominates from 0.65 V to 1 V. Figure 4a shows the kinetics obtained following a single wavelength (650 nm; corresponding to data plotted in a horizontal line across Fig. 2d) against time as the potential is changed from 0.6 V to different U values at 15 s and returned to 0.6 V at 60 s. The relative absorbance increases as charge is extracted and then decays as charge is injected when the potential is reversed. The rise and decay times of this signal are useful for understanding the kinetics of charges as they move from the back contact to drive interconversion of species at the interface and ultimately reach quasi-equilibrium (indicated by a plateau in ΔA). Confirmation that the kinetics observed is only related to the process of interest can be obtained by plotting the spectra at the plateau, Fig. 4b plots the spectra at 60 s (corresponding to a vertical line in Fig. 2d), normalized by peak wavelength. These are compared with $\overline{\Delta\alpha_1}(\lambda)$ as well as a spectrum obtained by increasing the upper potential to 1.1 V – beyond the window where process 1 dominates. Spectra within the

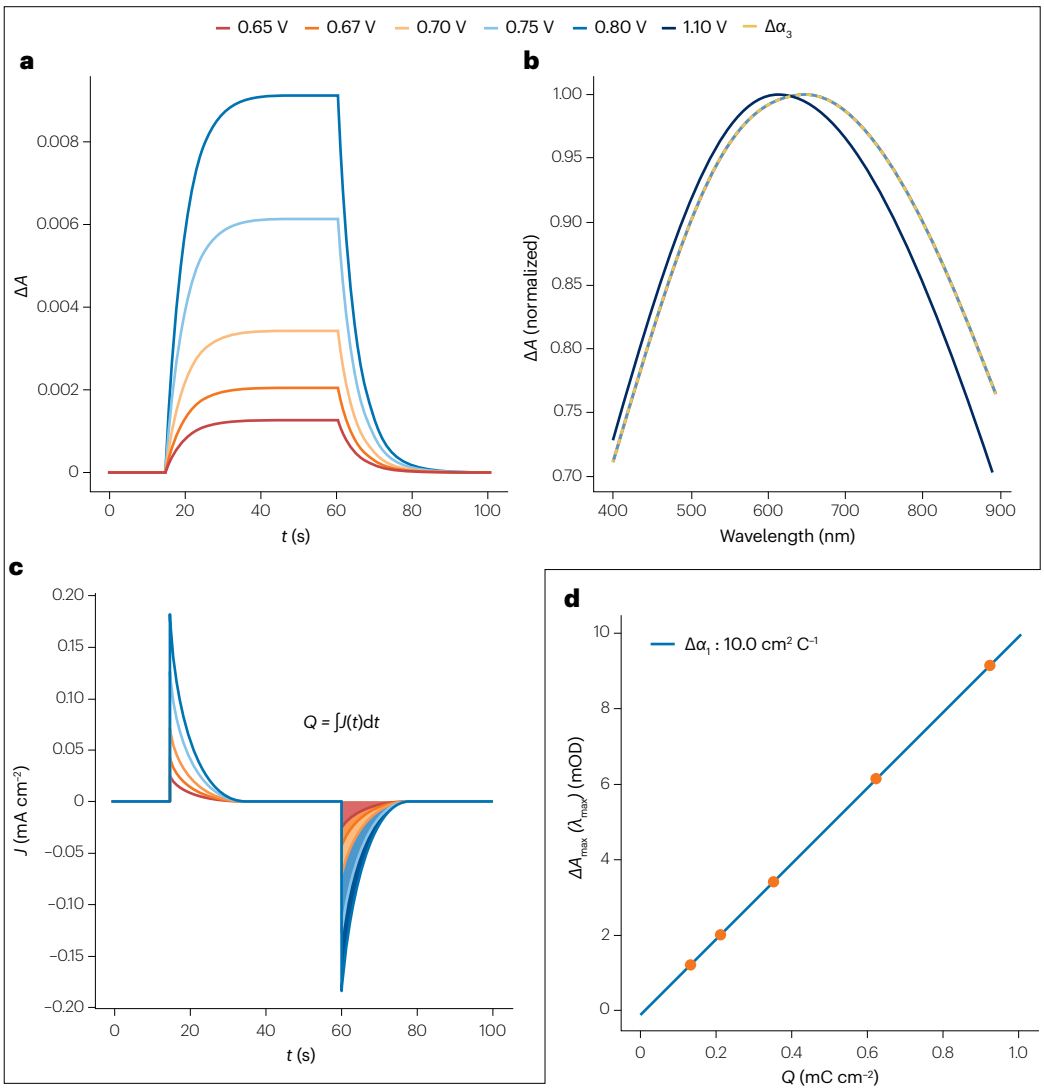

Fig. 4 | Example analysis of synthetic square-wave voltammetry-spectroelectrochemistry data. An example of square-wave voltammetry spectroelectrochemistry (SW-SEC) in a region in which a single process is occurring. A lower potential of 0.6 V is used. **a**, SW-SEC kinetics at 650 nm in the potential window dominated by redox process 1 (in which spectra from $\Delta\alpha_1$ dominate) with a lower potential of 0.6 V and at a series of upper potentials. **b**, Normalized spectra extracted at 60 s from the SW-SEC data shown in panel **a**, comparing the data with $\overline{\Delta\alpha_1}$. The upper potential of 1.1 V is outside the window in which process 1 dominates and so does not produce a spectrum that matches $\overline{\Delta\alpha_1}$. **c**, Current transients showing the measurement of charge associated with the potential step. The equation shows how charge can be extracted from the integration of the negative current transient, indicated by the regions of the curve that are filled in. **d**, Plot of the steady-state absorbance in part **a** plotted against the charge extracted in part **c**. The slope gives the value of $\Delta\alpha_1(\lambda_{max})$ by which $\overline{\Delta\alpha_1(\lambda)}$ can be scaled to give $\Delta\alpha_1(\lambda)$. For clarity, both the absorbance (optical density, OD) and the charge are scaled by 1,000 and expressed in units of milli-OD (mOD) and milli-coulombs (mC). All data shown in this figure are synthetic; details can be found in our GitHub archive.

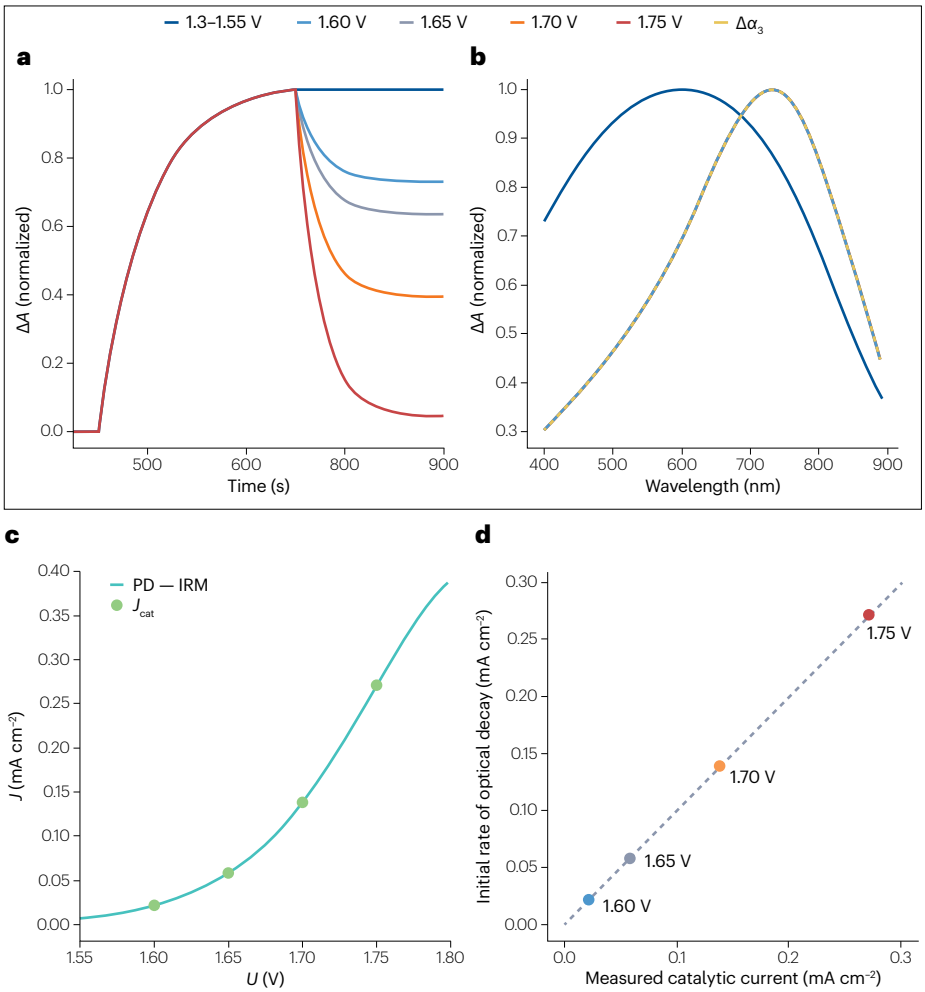

Fig. 5 | Example analysis of synthetic potential decay-spectroelectrochemistry data. An example of potential decay (PD)-spectroelectrochemistry (PD-SEC) collected in a window where only one process is occurring in comparison to a window of mixed processes. **a**, Normalized PD-SEC kinetics measured at 750 nm in the potential window where process 3 dominates (starting potential 1.55 V, series of step potentials) compared with the normalized kinetics in a potential window where process 2 dominates (1.3–1.55 V). **b**, Normalized spectra for the PD-spectroelectrochemistry extracted at 50 s compared with the normalized differential coulometric attenuation spectrum for process 3 ($\Delta\alpha_3$). **c**, Plot of the measured catalytic current (J_{cat}, obtained from subtracting capacitative current from the measured current) against potential, co-plotted with the current predicted from initial rate of the unnormalized PD (that is, using the initial rates method (IRM), converted to a current by dividing by $\Delta\alpha_3$). **d**, Plot of optically predicted currents against measured currents. All data shown in this figure are synthetic; details can be found in our GitHub archive.

window matching that of $\overline{\Delta\alpha_i}(\lambda)$ confirm that the kinetics belongs to this process. By contrast, the spectrum from outside the window does not correspond with $\overline{\Delta\alpha_i}(\lambda)$ and therefore should not be included in further analysis as it reports on mixed process kinetics.

SEC provides the shape of the differential coulometric attenuation coefficient ($\overline{\Delta\alpha_i}(\lambda)$) but not its magnitude ($\Delta\alpha_i(\lambda_{max})$). SW-SEC allows the calculation of this value as:

$$\Delta\alpha_i(\lambda_{max}) = \frac{\Delta A\left(\lambda_{max,t_{plateau}}\right)}{Q}.$$

$\Delta A(\lambda_{max,t_{plateau}})$ can be found from the peak value in each of the traces in Fig. 4a. Q can be obtained from the integration of the negative transient associated with the square wave (Fig. 4c). Here, a positive transient is observed as charge is extracted from the electrode, decaying to zero as quasi-equilibrium is reached. A negative transient is observed as the potential is reversed and charge is injected back into the system. For oxygen evolution, the positive charge stored in the electrode can ultimately drive the generation and the turnover of catalytic intermediates. As a result, in the case of a process generating a rate-limiting intermediate at catalytic potentials, the positive current transient will not decay to zero but rather to a constant value — corresponding to the steady-state rate of catalysis. This constant value complicates the integration of the transient to give charge. Consequently, it is standard practice to integrate the negative transient (Fig. 4c, filled in region) to give the charge stored[54]. A plot of the maximum absorbance against the charge stored (Fig. 4d) should form a straight line with a gradient of $\Delta\alpha_i(\lambda_{max})$. This value can then be used to convert the corresponding value of β_1 in Fig. 3d to a partial charge (Q_1).

PD-SEC

There is no guarantee that the process generating reactive intermediates will induce a change in UV–Vis absorbance. Furthermore, one, several or even all, optically observable processes occurring might catalytically produce inert products. To examine the reactivity of the products of a given process, potential windows where single processes dominate should be chosen for all processes occurring at or near catalytic potentials and PD-SEC experiments performed. The resulting kinetics should be normalized and the relative rates of decay are compared to provide insight into reactivity. Figure 5 demonstrates key PD-SEC plots that provide information into reactivity. Figure 5a shows kinetics obtained for potential windows corresponding to processes 2 and 3 shown in Fig. 3d. The normalized kinetics of process 2 does not decay even at an upper potential in which process 2 has

completed (corresponding to a potential step of 1.3–1.55 V), suggesting an inert state. By contrast, the products of process 3 decay even at upper potentials where process 3 is far from completion (1.55–1.6 V), suggesting reactivity. As with SW-SEC, it is important to check that the species generated by the potential step produce the same spectrum as the differential attenuation coefficient for the process being examined (Fig. 5b). It is also advisable to analyse the spectral signatures arising from the decay of the signal under open circuit (that is, $\Delta A_{\mathrm{decay}} = \Delta A_{t>50\mathrm{s}} - \Delta A_{t=50\mathrm{s}}$), which should also correspond to the reversal of the process as catalytic turnover should generate states earlier in the catalytic cycle, leading to an optical spectrum equivalent to reversing the process that generates a rate-limiting intermediate[23].

Once it has been confirmed that the rise and decay of the signal can be attributed to the generation (and subsequent consumption) of product of a single process, the initial rate of decay of the signal can be used to assay the rate of the reaction. Initial rates can either be obtained through linear fitting of the early part of the decay or, if signals are much greater than noise, through a numerical derivative. The self-discharge current that this optical decay corresponds to is:

$$J_{\mathrm{cat}}^{\mathrm{optical}} = \left| \frac{\mathrm{d}Q}{\mathrm{d}t} \right| = \left| \frac{\mathrm{d}\Delta A(\lambda)}{\mathrm{d}t} \times \frac{1}{\Delta\alpha_i(\lambda)} \right|.$$

If the product generated by a process is responsible for driving catalysis, $J_{\mathrm{cat}}^{\mathrm{optical}}$ should be commensurate to the catalytic current measured. The measured current, J, contains both a capacitive and a catalytic contribution. To compare J with $J_{\mathrm{cat}}^{\mathrm{optical}}$, the capacitive contribution must be subtracted or otherwise removed. This can be measured by applying fixed potential as a function of time until a steady-state catalytic current is observed (this measurement is known as chronoamperometry – note that chronoamperometry might be unsuitable for materials with good short-term stability, but suitable for those with poorer long-term stability as repeated holds at a series of potentials give the system more time to degrade than a single potential sweep), or approximated by subtracting out the faradaic capacitive current using CV-SEC data, which gives $Q_i(U)$. In this case:

$$J_{\mathrm{cat}} \approx J - \frac{\mathrm{d}Q_{\mathrm{cap}}(U)}{\mathrm{d}U} \times \nu,$$

in which $Q_{\mathrm{cap}}(U) = \sum_i^N Q_i(U)$ and the scan rate – a constant for a cyclic voltammogram – is $\nu = \frac{\mathrm{d}U}{\mathrm{d}t}$. From this, the degree to which an intermediate can support the measured current can be approximated. Figure 5c superimposes the optical decay current on top of the J versus U curve and shows the extent to which the optically extracted current follows the trend of the measured current. Figure 5d directly plots optical and measured currents against one another and is a useful visualization of systemic overestimation or underestimation associated with deviation from a slope of 1. It is worth noting that self-discharge processes can involve the same chemical step that occurs under applied potential and show a slightly different rate owing to changes in the double layer that might occur when the circuit is opened[23,55,56]. For gold-standard proof of chemical reactivity, PD-SEC should couple with a technique that senses the rate of evolution of products. For the example of the OER, the rate of optical decay should be four times the rate of oxygen evolution under the same conditions[23] as, for a full catalytic turnover, four electrons are transferred for each optically measured rate-determining transfer. With proof that an intermediate does indeed drive the reaction, the intrinsic rate of the reaction (reaction rate of the rate-limiting intermediate) can be calculated provided the number of electrons involved in the catalytic cycle is known. In the case of OER, in which four electrons are needed for one turnover:

$$V(U) = \frac{J_{\mathrm{cat}}(U)}{4Q_{\mathrm{RLI}}(U)}.$$

This value is broadly analogous to the TOF measured in molecular catalysis, with the caveat that TOF is commonly calculated by normalizing against the total number of moles of a catalyst introduced to the system. We use the term intrinsic rate to distinguish the fact that the normalization is performed against the density of rate-limiting intermediates available at a given potential.

Applications

In this section, we outline how the parameters extracted from the three SEC techniques outlined earlier can be used in the example of OER electrocatalysis and highlight broader examples in energy materials.

Measurement of binding energy in electrodes

A process generating an intermediate that turns over at a rate commensurate to the rate of catalysis and is generated faster than it is consumed provides evidence to support the assignment of a rate-limiting, surface-bound intermediate existing in a state of quasi-equilibrium. On the grounds of this assumption (and that the process generating this intermediate is the last observed in the window), the degree of completion σ can be related to the surface coverage of the rate-limiting intermediate (θ) and its standard potential is referred to as the binding energy or binding strength. The relation of coverage to potential is referred to as an electroadsorption isotherm.

Binding energy has an important role in controlling the rate of inner-sphere electrocatalytic reactions. This is because of a strong correlation to the activation energy of the rate-limiting step that consumes that intermediate (which is described by the Brønsted–Evans–Polanyi principle)[57–59]. In multistep reactions in which the substrate is bound to the catalyst through the same atom in each step (for example, in OER as shown in Fig. 1a), this importance is undiminished, as the binding energy associated with each of the step scales linearly with the subsequent step (the so-called scaling relations)[59–62]. These two effects lead to volcano relations, in which a clear optimum in intrinsic rate is found for a rate-limiting intermediate between the extremes of strong and weak binding.

Although volcano relations are strongly predictive of activation energy and activity in theory, experimentally derived optimum intrinsic rates have been weaker than expected for OER[63]. This might arise from the fact that binding energies are typically calculated using density functional theory (DFT) on pristine single-crystal facets and do not consider coverage effects. Experimental catalysts present multiple facets to the surface and might have little or no crystallinity or exhibit strong interactions with ions and molecules in the double layer[20,21,23]. These interactions can introduce changes in binding energies that are challenging to simulate in the absence of experiment. In the simplest case, coverage dependency of the binding energies can be represented by modifying the Langmuir (Nernstian) isotherm with an additional linear term:

$$U = U^{\ominus} + \frac{RT}{F}\mathrm{Ln}\left(\frac{\sigma}{1-\sigma}\right) + \frac{r\sigma}{F}.$$

This equation, known as the Frumkin adsorption isotherm, adds an additional parameter, r – the marginal molar adsorption enthalpy increase that arises from a monolayer of coverage of a given adsorbate. In this case, the binding energy of the rate-limiting intermediate is no

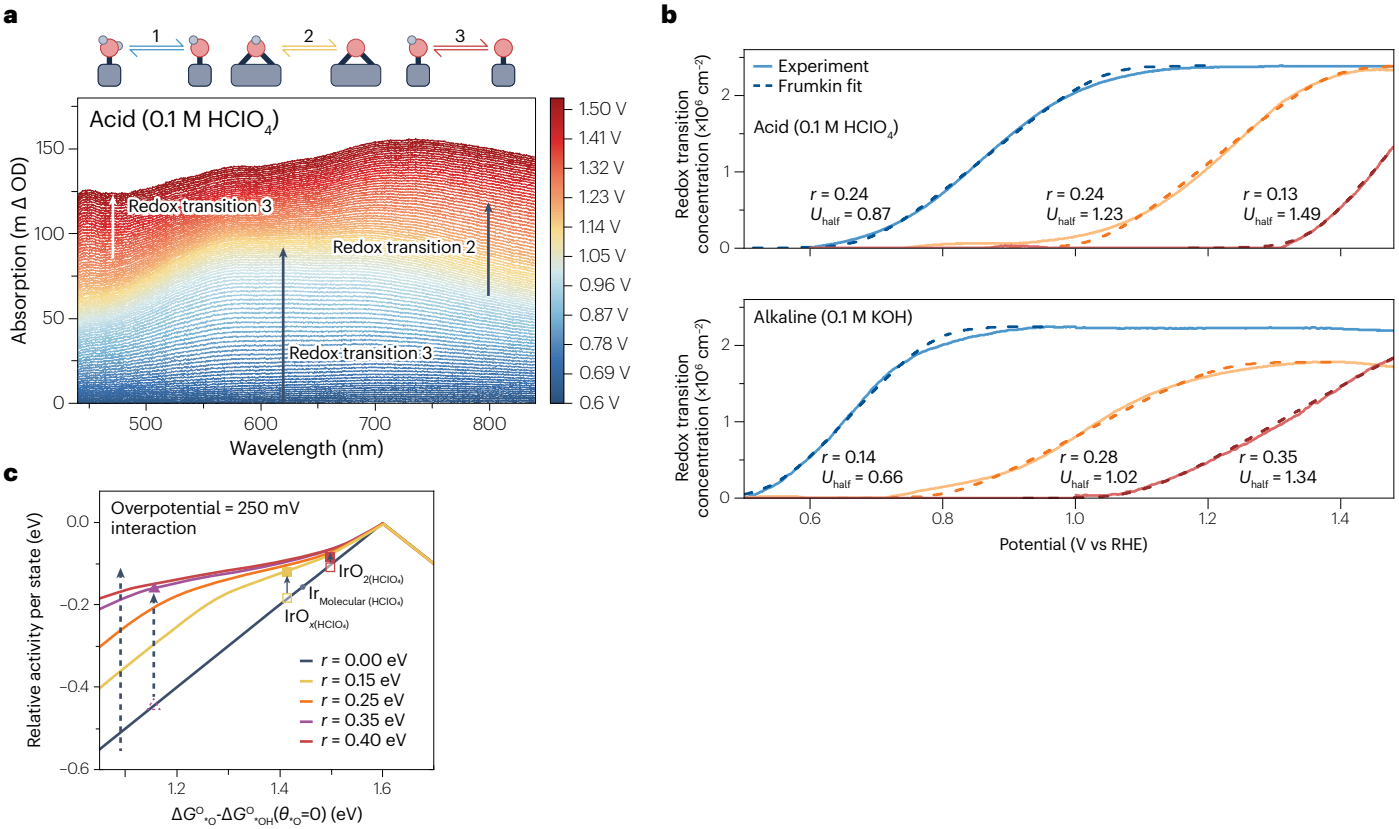

Fig. 6 | Extraction of the binding and interaction energy from the rate-limiting intermediate for oxygen evolution reaction in iridium oxide. **a**, Spectroelectrochemistry collected from an amorphous IrO_x sample in an acidic electrolyte showing regions clearly dominated by different processes. **b**, The results of attenuation, spectral extraction and linear fitting scaled by the maximum value of the attenuation coefficients. In this case, the partial charge is converted to a surface concentration using Faraday's and Avogadro's constants and assuming a one-electron process with a reactant: product stoichiometry of 1:1. **c**, Modified volcano plot measured at fixed overpotential, which includes the effect of adsorbate interactions. The *x* axis is the binding energy in the absence of interactions. The binding energy is the redox potential where coverage increases the fastest with increasing potential. Thus, systems with lower values of binding energy have higher coverage at an overpotential of 250 mV (that is, 1.48 V versus reversible hydrogen electrode (RHE)). If a large *r* value is observed, then this high coverage will modify the overall binding energy towards the optimum (*y* axis: distance from the optimum binding energy in electronvolts). For clarity, the absorbance (optical density, OD) is scaled by 1,000 and expressed in units of milli-OD (mOD). Parts **a** and **b** reprinted from ref. 21, CC BY 4.0. Part **c** reprinted from ref. 23, CC BY 4.0.

longer constant and is instead a linear function of coverage ($U^{\ominus} + \frac{r\sigma(U)}{F}$). The volcano optimum can therefore be reached in strongly bound materials with a large enough *r* at significant coverage.

The techniques discussed earlier have been used to extract binding and interaction energies from complex and disordered materials, such as amorphous iridium oxide[21,23]. SEC of this material indicates the presence of three redox processes (Fig. 6a). Commensurate partial charges for each of the three redox processes were observed. This result is comparable with single-crystal studies in which three processes are observed arising from μ_1 and μ_2 sites in a 1:1 stoichiometry and assigned identically to Fig. 1c. Using DFT provided corroboration of the mechanism and the order of the processes, in which process 1 was described as $\mu_1{*}OH_2 \rightarrow \mu_1{*}OH$, process 2 $\mu_1{*}OH \rightarrow \mu_1{*}O$ and process 3 $\mu_2{*}OH \rightarrow \mu_2{*}O$ (Fig. 6a, top). Given this domain knowledge assignment, the coverage of process 3 (which did not complete in the potential window studied) could be estimated as $\sigma_3(U) = \theta_3(U) = \frac{Q_3(U)}{Q_{2,\max}}$, as this mechanistic interpretation takes μ_2 and μ_1 sites to exist in a 1:1 ratio. From this, the degree of completion of all three processes was plotted and fitted to Frumkin isotherms (Fig. 6b, top). For the final equilibrium where coverage and completion are approximately equivalent, the rate-limiting intermediate was found to generate non-negligible interaction energies of 0.13 eV. This finding indicates that increasing coverage to 100% will destabilize binding by 0.13 eV. Intriguingly, *r* was found to triple under alkaline conditions (Fig. 6b, bottom). In this case, a far lower standard potential was observed, implying that more destabilization is required to reach the optimum, effectively countering the increased *r* value. PD-SEC coupled with in situ electrochemical mass spectrometry indicated that the third process generates a rate-limiting intermediate that decays at a rate commensurate to both the current and the rate of O_2 generation – proving that the intermediate measured by SEC drives reaction, and thus, that the measured binding and interaction energies dictate activity. Plotting the modified volcano relation (Fig. 6c) at a fixed overpotential shows that in both acidic and alkaline conditions, IrO_x exhibited binding close to the volcano optimum but for different reasons. Under acidic conditions, the binding energy in the absence of disruption of interactions that stabilize the interface

was closer to the 1.6 V versus reversible hydrogen electrode optimum. A modest value of r brings this value closer to the optimum for the value of $\theta(U)$ at this overpotential. By contrast, in alkaline conditions, binding began as too weak and was rapidly driven to the optimum by the large value of r.

Tafel slope reconstruction in electrodes with coverage-dependent adsorption enthalpies

The Tafel slope describes the slope in a plot of the overpotential for the reaction against the log of the current density and is an important performance metric for a catalyst. Tafel slopes can be used for microkinetic models that assume the number of equilibria needed to form the rate-limiting intermediate and fit by tuning the intrinsic rate of reaction and standard potentials of pre-equilibria[64]. A common assumption in such models is that the coverage of the rate-limiting intermediate follows a Langmuir (Nernstian) adsorption isotherm. However, in the case of strong interaction energies, this fitting can be strongly affected, leading to misleading mechanistic conclusions. This was highlighted by SEC experiments investigating CoOOH[20]. A strong fit of the CV-SEC data for CoOOH (Fig. 7a, top panel) was evidenced by the fact that the calculated capacitate current strongly matched the measured capacitate current (Fig. 7a, bottom panel). However,

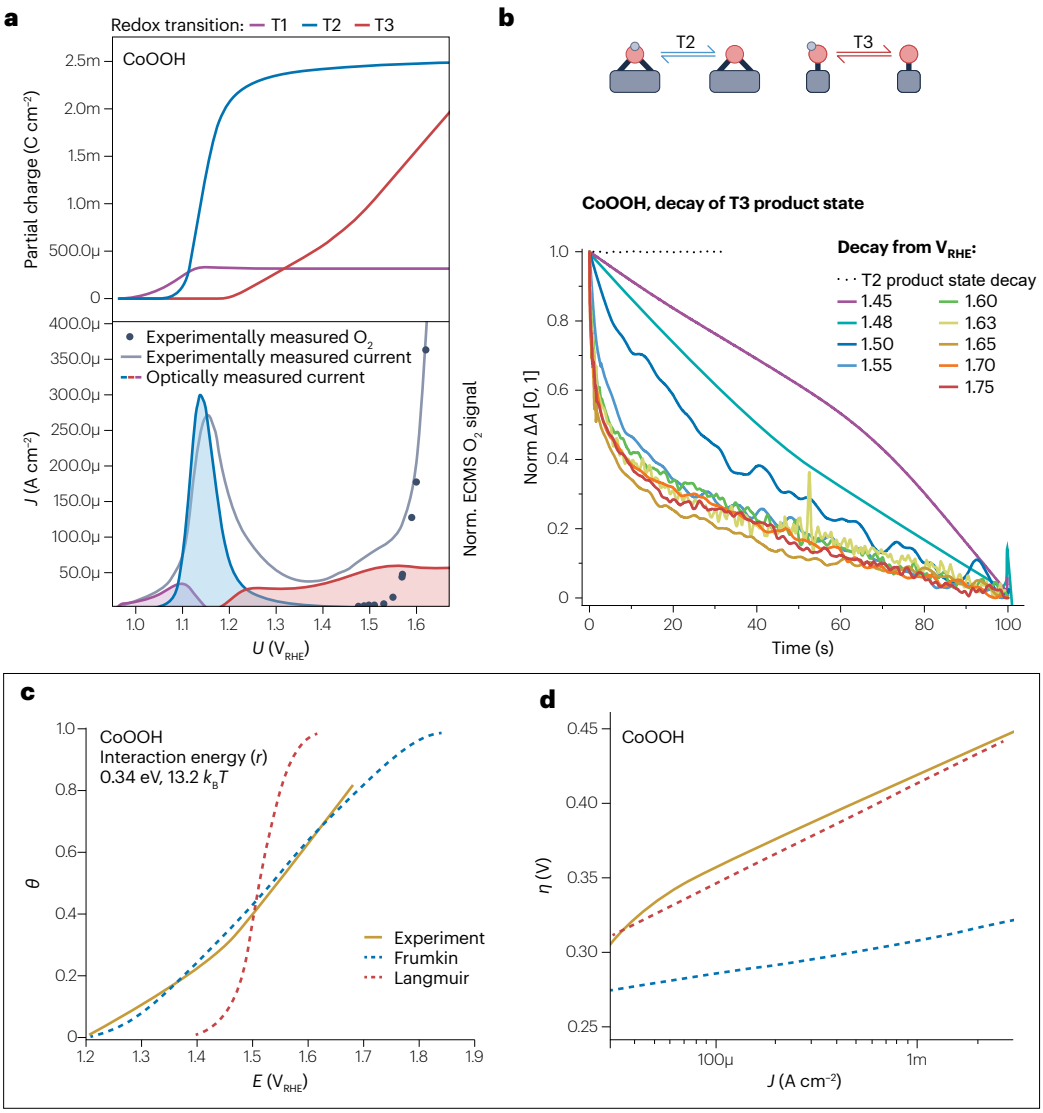

Fig. 7 | Tafel slope reconstruction using optical data in cobalt oxyhydroxide (CoOOH) oxygen evolution reaction catalysts. a, Top: results of fitting spectroelectrochemistry data with results converted into a partial charge. Bottom: results converted into a changing current, co-plotted with the measured current (grey line) and oxygen generation measured by in situ electrochemical mass spectrometry (ECMS, black dots). **b**, Normalized potential decay-spectroelectrochemistry decay kinetics of the third process (T3), showing a 100-fold increase in the initial rate of decay with increasing applied potential. The black dotted line shows the decay kinetics associated with the previous process (no decay). **c**, The coverage of process T3 (the final process in the system, thus $\sigma = \theta$) fitted against Langmuir and Frumkin adsorption isotherms. **d**, Tafel slopes reconstructed using the fitted Frumkin dependence of coverage on potential against that predicted when the best-fitting Langmuir dependence is used. The resulting interaction energy r is 0.13 eV, or 13.2 times Boltzmann's constant room temperature (k_BT). RHE, reversible hydrogen electrode. Adapted from ref. 20, CC BY 4.0.

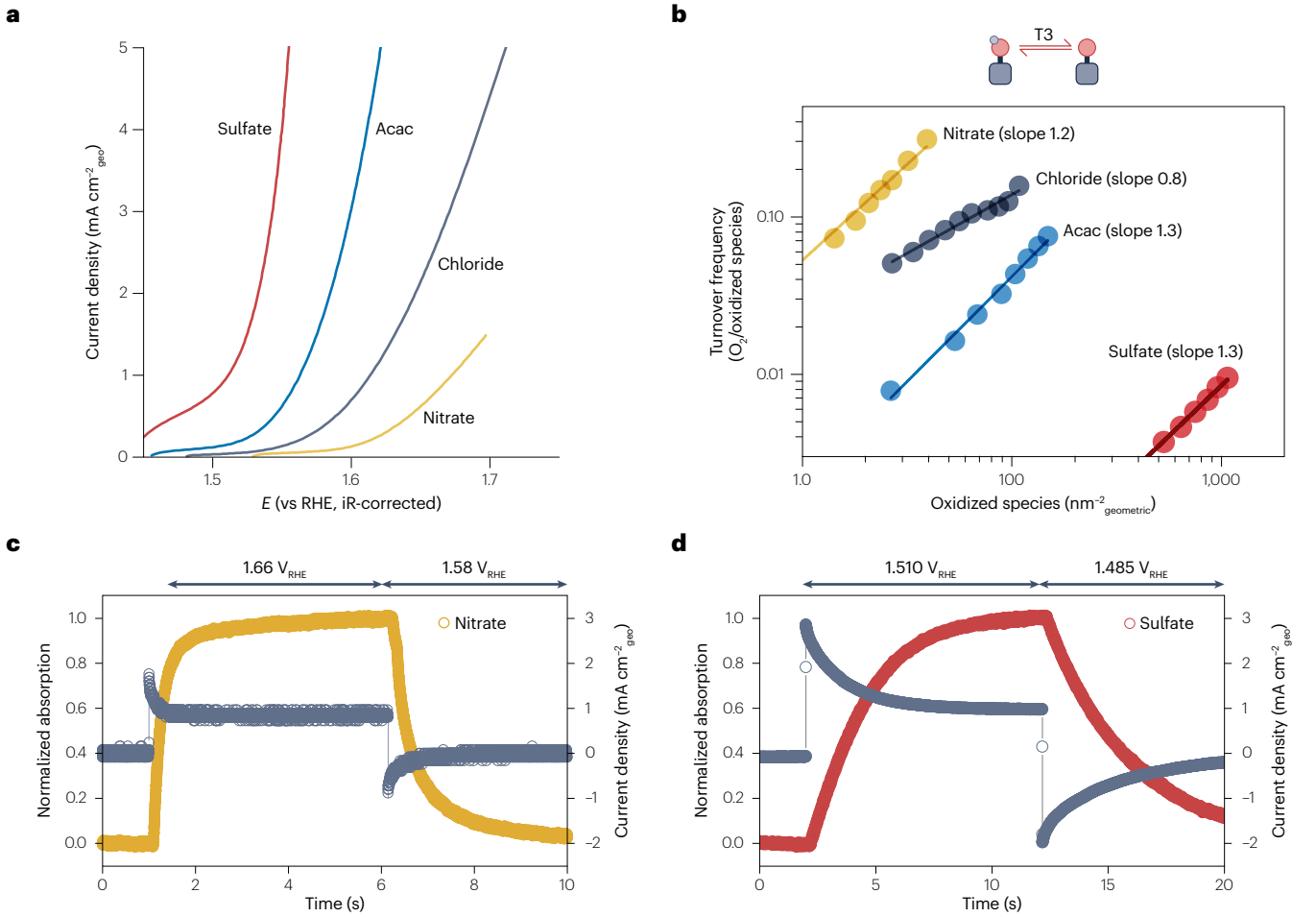

Fig. 8 | Active state quantification and analysis of charging/discharging kinetics in iron-incorporated nickel oxyhydroxide (NiFOOH) oxygen evolution reaction catalysts. a, Current voltage curves of Ni(Fe)OOH nanoparticles synthesized in the presence of an anion that modifies the size of the particle. **b**, Plot of the turnover frequency against the partial charge, represented as a number of species assuming 1:1 reactant–product stoichiometry. **c**,**d**, Square-wave voltammetry-spectroelectrochemistry kinetics of the catalytically active species for oxygen evolution reaction, showing fast charging and discharging for nitrate-derived particles (part **c**) and slow charging for sulfate-derived particles (part **d**) upon application of a square-wave potential measured versus a reversible hydrogen electrode (RHE) reference. Reprinted from ref. 22, CC BY 4.0.

the third and final process measured started long before OER current or oxygen evolution was observed (Fig. 7a, bottom panel, grey line and black dots). The intuitive indication that this intermediate is not associated with catalysis was disproven by PD-SEC kinetics, which showed a two-order-of-magnitude acceleration of the rate of decay of the intermediate associated with this process as potentials were increased (Fig. 7b). This is consistent with the rate of increase in current and oxygen generation, implicating these states in catalysis. This was confirmed by the large interaction parameter of 0.37 eV, which produced a Frumkin isotherm with behaviours far from the ideal Langmuir behaviour. A result of this is that using the best fit of the Langmuir isotherm density did not reproduce the Tafel slope, given the experimentally determined dependence of current on coverage (Fig. 7c). Only by introducing the additional coverage effect of a Frumkin isotherm could the experimentally determined current/coverage relation be reconciled without introducing rates of reaction inconsistent with the coverages measured (Fig. 7d).

Measurement of process-specific charging and discharge rates

A considerable challenge in electrochemical conversion technologies are disentangling extrinsic factors, such as the surface area and number of available reactive sites, from intrinsic factors such as TOF and conductivity. An example[22] of how this can be achieved is shown in Fig. 8. Here, Fe-doped NiO nanoparticles were synthesized in the presence of four anions, which strongly affected the particle size and thus surface area. The current potential curve (Fig. 8a) shows a trend of increasing activity with precursors that reduce particle size. However, the calculation of TOF as a function of reactive available sites removes this trend (Fig. 8b). One of the key contributors to the trend could be the conductivity of the film reflected in the SW-SEC kinetics, as despite being of commensurate thickness, films composed of larger particles (Fig. 8c) show far faster rise and decay kinetics than those composed of the smallest particles (Fig. 8d). In the latter case, the charge injection and extraction times are slow enough for resistivity and charge transport to become a relevant consideration.

Emerging applications

One of the key advantages of the SEC configuration discussed herein is that the speed of collection enables the study of materials that are too unstable to be studied by other means. Additionally, the resolution means that irreversible processes, which cannot be accurately resolved by averaging spectra together, can be resolved in a single pass. An example of the former case is the non-fullerene electron acceptor molecules used in organic photovoltaics[18] (such as ITIC, as shown in Fig. 9a). It would be desirable to distinguish the optical spectrum of the reduced form of these materials to be able to track the formation of anions from neutral charge-separated states using other techniques. However, these materials are optimized for operation in solid-state devices, and electrochemical reduction in electrolyte induces rapid degradation. The rapid acquisition of SEC data enabled the spectra of anions to be acquired in seconds before a considerable degree of film degradation (Fig. 9b).

The ability to collect high-resolution, time-resolved spectra in a single pass has provided insights into the degradation processes of organic materials with complex electrochemical interfaces. For example, the series of polymers in Fig. 9c can be used to make organic electrochemical transistors. These materials suffer from degradation during operation, which is challenging to assess in situ. Using PD-SEC (Fig. 9d), a single-charge injection-decay event was successfully resolved, showing that polymers with a higher conduction band energy exhibit faster decay rates. By excluding oxygen, decay was completely supressed, implicating electron transfer to oxygen as the mechanism for degradation.

Reproducibility and data deposition

Performant SEC systems must currently be built rather than purchased, and differences in components, analysis or code can induce a difference in results. For example, SEC can be performed both by programming a potential sweep and continuous acquisition (as suggested herein) or by a loop involving incrementing the potential, then reading the current and the spectrum. Such a difference will introduce subtle changes in the measured current, the number of acquisitions and the potentials

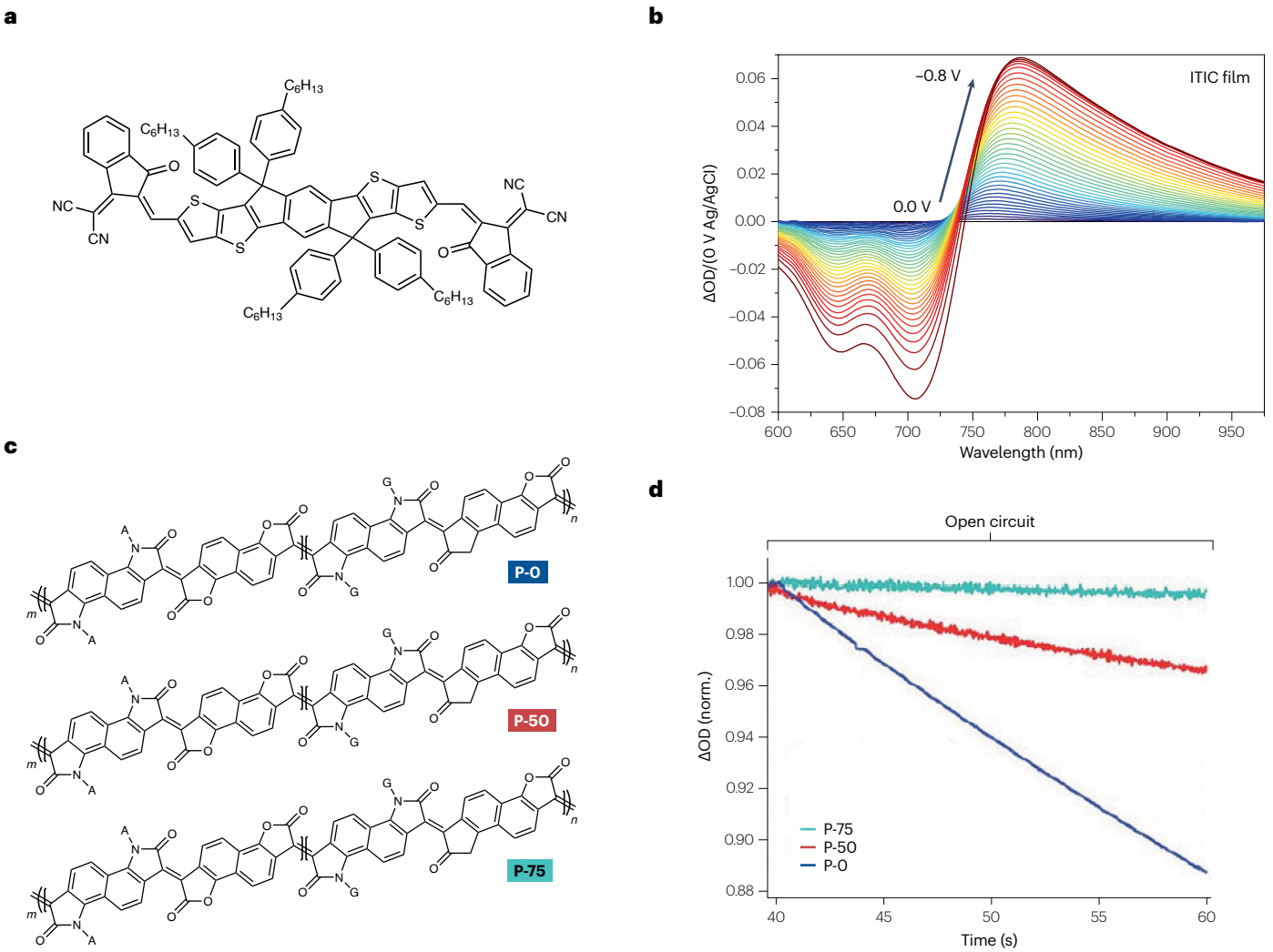

Fig. 9 | Measurement of the spectra of charged ions of materials used in photovoltaics and organic electrochemical transistors. a, The structure of ITIC, a non-fullerene acceptor molecule. **b**, The spectrum of anions of ITIC generated by the forward scan of a fast cyclic voltammetry-spectroelectrochemistry experiment. **c**, A series of polymers, shown in order of decreasing conduction band energy. **d**, Potential decay-spectroelectrochemistry experiments showing the relative decay rates of generated anions. OD, optical density. Parts **a** and **b** adapted from ref. 18, CC BY 3.0. Parts **c** and **d** reprinted from ref. 19, CC BY 4.0.

associated with an acquisition. The choice of the experiment design is not always freely made owing to the varying capabilities of the programming interfaces available for each individual component and the programming language chosen for automation. We therefore recommend readers devise a benchmark sample to ensure validity. Internally, we use electrodeposited IrO_x films (described in ref. 23) to ensure that results are consistent across laboratories.

A challenge to open and comparable data is that the raw data generated by a single SEC experiment can be several gigabytes in size. An appropriate downsampling procedure (such as downsampling to 1 nm and 1 mV per acquisition by adjacent averaging) must be performed. If the experiment is relatively small, the downsampled data can be written to a text format (such as .txt or .csv) and directly uploaded to a repository such as GitHub or Zenodo. For larger experiments such as an SEC experiment containing many cycles, further compression and partitioning might be required. A useful compressed format is Apache Parquet, a columnar format that supports extensive compression and is simple to partition into subfiles (containing subsets of cycles or scans) and subsequently load and reconstruct.

Limitations and optimizations

One of the key limitations and causes of confusion in the literature is the loss of information about the absolute populations associated with a process, which occurs when working with relative absorbance and in cases in which absorptivity spectra strongly overlap. This lack of information means that microkinetic models of the system cannot be assembled from partial charge or the degree of completion without additional information. In the example synthetic data herein, three processes occur. The interpretation of these processes into populations or coverages requires domain knowledge of stoichiometry. Limiting the discussion to 1:1 reactant: product stoichiometries and single-electron oxidations, the three processes could be interpreted as:

$$A \rightarrow B + e^- \rightarrow C + 2e^- \rightarrow D + 3e^-, \quad (1)$$

$$A \rightarrow B + e^- \rightarrow C + 2e^-, D \rightarrow E + e^-, \quad (2)$$

$$A \rightarrow B + e^-, C \rightarrow D + e^-, E \rightarrow F + e^-, \quad (3)$$

In the case of the sequential mechanism (equation (1)), the completion of a process implies the consumption of the products of the prior process. In equation (3), all three processes occur in tandem, meaning the products of each process can coexist even when all processes have completed. Mixed tandem and sequential mechanisms such as those shown in equation (2) are also possible. For the final process in each case, the degree of completion and the coverage are equivalent. However, the coverage and degree of completion for mechanisms shown in equations (1) and (2) are not equivalent for any of the prior processes. In the case shown in equation (3), the microkinetic coverage is equivalent to the degree of completion as the equilibria are independent:

$$\theta_B = \sigma_{A\rightarrow B}, \theta_D = \sigma_{C\rightarrow D}, \theta_F = \sigma_{E\rightarrow F}.$$

However, in the sequential mechanism (shown in equation (1)), the products of each equilibrium are the reactants for the next:

$$\theta_B = \sigma_{A\rightarrow B} - \sigma_{B\rightarrow C}, \theta_C = \sigma_{B\rightarrow C} - \sigma_{C\rightarrow D}, \theta_D = \sigma_{C\rightarrow D}.$$

If it can be reliably assumed that each process corresponds to a one-electron oxidation, and that there is a 1:1 reactant–product stoichiometry in each step, an equal completing charge (Q_T, i) of each process indicates that all sites undergoing reaction also exist in 1:1 stoichiometry. This could distinguish a polycrystalline interface with one predominant facet from, for example, a polycrystalline interface where exposed facets occur in different ratios, with each process belonging to a specific facet. Another reason for a deviation from 1:1 stoichiometries is that SEC is not inherently a surface-specific technique. If one or more of the redox processes penetrate beyond the interface into the bulk of the material, then different completing charges will be observed and the potential for the surface-specific process will become harder to discern from the large signal of bulk processes. This hypothesis is best interrogated using complementary experiments to reveal the structure of films, the electrochemical accessibility of sites, porosity of the films and the relative penetration of redox processes into them[23,26,46,65]. Regardless of the system or level of domain knowledge, assumptions of 1:1 stoichiometry between processes or 1:1 reactant: product stoichiometry within processes should be explicitly stated.

An additional limitation of UV–Vis spectroscopy of solid interfaces is that transitions often do not typically arise from individual atomic orbitals or states, but rather occur from a continuum of states (band-to-band transitions). These transitions are broad in comparison to molecular absorption spectra and often lack simple and specific molecular information. This strongly increases the chances of large overlap in the absorptivity spectra (Supplementary Box 1). Furthermore, differential attenuation coefficients are related to the difference between two sets of transitions rather than a single set of transitions. In the absence of additional information, a molecular interpretation of the difference spectra that arise in complex solid interfaces should therefore be avoided, as spectra are so complex as to contain no chemical information. Rather, differential spectra should be seen as fingerprints of processes that provide no direct information about stoichiometry. For example, the reactions $A \rightarrow B + e^-$, $A \rightarrow 2B + e^-$ and $A \rightarrow B + C + e^-$ will have the following differential attenuation spectra, respectively:

$$\Delta\alpha = \alpha_B - \alpha_A,$$

$$\Delta\alpha = 2\alpha_B - \alpha_A,$$

$$\Delta\alpha = \alpha_B + \alpha_C - \alpha_A.$$

Without domain expertise or additional measurement of the chemical nature of reactants and products, these processes cannot be distinguished from one another using SEC. Despite the ubiquity of invoking 1:1 reactant–product stoichiometries involving the single-electron oxidation of only one atom, assumptions of the stoichiometry and number of electrons should be explicitly stated so that the microkinetic interpretations of spectra can be revised if new evidence comes to light.

Finally, there is no guarantee that either the reactants or products involved in a process will absorb in the UV–Vis region. SEC data should therefore be shown (rather than assumed) to track most of the processes occurring in a material by demonstrating that the reconstructed capacitative charging current from SEC explains the measured current (Fig. 7a, bottom). Beyond these key considerations for interpreting data, other experimental considerations are required to produce valid, interpretable data. These can be found in Supplementary Table 1.

Outlook

Developments in computing power, open-source programming languages and detector technology have produced a step change in what

can be accomplished with operando UV–Vis SEC. An outstanding challenge in the field of high throughput and automated chemistry is the need to collect information on interfaces that can only be characterized in situ. The balance of accessibility, sensitivity and data volume makes SEC a highly versatile technique for the collection of large-volume and high-throughput data. SEC provides detailed information about the potentials at which processes occur, as well as the density and reactivity associated with the products of a process. However, a key limitation of the technique is that it provides no direct chemical insights into the nature of the reactants and products generated by a process. In the future, we anticipate that the unique weaknesses and strengths of SEC can be mitigated and enhanced, respectively, by directly coupling the technique with highly automated, multimodal, high-throughput measurement systems. For example, detailed information about the relation of reversible oxidation processes to irreversible corrosion could be obtained by coupling SEC with in-line inductively coupled plasma mass spectrometry. Similarly, coupling SEC to techniques that provide deep chemical insights but have slow acquisition times (such as X-ray absorption and Raman spectroscopies) could provide a holistic view of the chemical species that are interconverted by the processes monitored in SEC. The slower techniques could take 'snapshots' of chemical nature of system at potentials where processes begin and complete. Advanced computational tools could also provide the chemical insights needed to complement the detailed dynamics provided by SEC. For example, the PyTASer package[66] uses DFT to simulate the differential attenuation coefficients associated with different chemical processes. A match of a simulated and measured value would provide strong evidence of the chemical nature of a process. A barrier to these aims is the lack of standardization of operating software and analysis procedures. To facilitate the general use of SEC, open-source operating software should be developed that can be easily understood and adapted to the ends of the user, who can then analyse their results using open-source analysis scripts that have been vetted and optimized by a community of users. Recent developments in this space such as highly modular, Python-based webserver orchestrators[67] and open-source operando analysis packages such as ixdat have paved the way for robust and flexible community-driven software, whereas advances in 3D printing have removed the need for (and expense of) machining expertise. Taken together, we anticipate a future where the rapid prototyping of innovative cell designs and optical configurations can be coupled with rapid experiment automation.

Published online: 20 November 2025

References

1. Kim, T., Song, W., Son, D.-Y., Ono, L. K. & Qi, Y. Lithium-ion batteries: outlook on present, future, and hybridized technologies. *J. Mater. Chem. A* **7**, 2942–2964 (2019).
2. Liu, T. et al. Current challenges and routes forward for nonaqueous lithium-air batteries. *Chem. Rev.* **120**, 6558–6625 (2020).
3. Burke, M. S., Enman, L. J., Batchellor, A. S., Zou, S. & Boettcher, S. W. Oxygen evolution reaction electrocatalysis on transition metal oxides and (oxy)hydroxides: activity trends and design principles. *Chem. Mater.* **27**, 7549–7558 (2015).
4. Chung, M. et al. Direct propylene epoxidation via water activation over Pd–Pt electrocatalysts. *Science* **383**, 49–55 (2024).
5. Chang, W., Jain, A., Rezaie, F. & Manthiram, K. Lithium-mediated nitrogen reduction to ammonia via the catalytic solid–electrolyte interphase. *Nat. Catal.* **7**, 231–241 (2024).
6. Twight, L. et al. Trace Fe activates perovskite nickelate OER catalysts in alkaline media via redox-active surface Ni species formed during electrocatalysis. *J. Catal.* **432**, 115443 (2024).
7. Sharpe, L. R., Heineman, W. R. & Elder, R. C. EXAFS spectroelectrochemistry. *Chem. Rev.* **90**, 705–722 (1990).
8. Zheng, W. Beginner's guide to Raman spectroelectrochemistry for electrocatalysis study. *Chem. Methods* **3**, e202200042 (2023).
9. Li, J. et al. Ultrasensitive plasmon-enhanced infrared spectroelectrochemistry. *Angew. Chem. Int. Ed.* **63**, e202319246 (2024).
10. Nemes, C. T., Swierk, J. R. & Schmuttenmaer, C. A. A terahertz-transparent electrochemical cell for in situ terahertz spectroelectrochemistry. *Anal. Chem.* **90**, 4389–4396 (2018).
11. Colburn, A. W., Levey, K. J., O'Hare, D. & Macpherson, J. V. Lifting the lid on the potentiostat: a beginner's guide to understanding electrochemical circuitry and practical operation. *Phys. Chem. Chem. Phys.* **23**, 8100–8117 (2021).
12. Selim, S. et al. Impact of oxygen vacancy occupancy on charge carrier dynamics in $BiVO_4$ photoanodes. *J. Am. Chem. Soc.* **141**, 18791–18798 (2019).
13. Barroso, M. et al. Dynamics of photogenerated holes in surface modified α-Fe_2O_3 photoanodes for solar water splitting. *Proc. Natl Acad. Sci. USA* **109**, 15640–15645 (2012).
14. Moss, B. et al. Linking in situ charge accumulation to electronic structure in doped $SrTiO_3$ reveals design principles for hydrogen-evolving photocatalysts. *Nat. Mater.* **20**, 511–517 (2021).
15. Astuti, Y. et al. Proton-coupled electron transfer of flavodoxin immobilized on nanostructured tin dioxide electrodes: thermodynamics versus kinetics control of protein redox function. *J. Am. Chem. Soc.* **126**, 8001–8009 (2004).
16. Astuti, Y., Topoglidis, E., Cass, A. G. & Durrant, J. R. Direct spectroelectrochemistry of peroxidases immobilised on mesoporous metal oxide electrodes: towards reagentless hydrogen peroxide sensing. *Anal. Chim. Acta* **648**, 2–6 (2009).
17. Bevan, A. W. et al. Cyclic voltammetry and spectroelectrochemistry of two common thiophene polymers reveals ion diffusion and polaron wave function extent. *Chem. Mater.* **37**, 1949–1960 (2025).
18. Guo, J., Moss, B. & Clarke, T. M. Quantifying triplet formation in conjugated polymer/non-fullerene acceptor blends. *J. Mater. Chem. A* **10**, 20874–20885 (2022).
19. Alsufyani, M. et al. The effect of organic semiconductor electron affinity on preventing parasitic oxidation reactions limiting performance of n-type organic electrochemical transistors. *Adv. Mater.* **36**, e2403911 (2024).
20. Moss, B. et al. Cooperative effects drive water oxidation catalysis in cobalt electrocatalysts through the destabilization of intermediates. *J. Am. Chem. Soc.* **146**, 8915–8927 (2024).
21. Liang, C. et al. Role of electrolyte pH on water oxidation for iridium oxides. *J. Am. Chem. Soc.* **146**, 8928–8938 (2024).
22. Rao, R. R. et al. Unraveling the role of particle size and nanostructuring on the oxygen evolution activity of Fe-doped NiO. *ACS Catal.* **14**, 11389–11399 (2024).
23. Liang, C. et al. Unravelling the effects of active site density and energetics on the water oxidation activity of iridium oxides. *Nat. Catal.* **7**, 763–775 (2024).
24. Lee, S., Moysiadou, A., Chu, Y.-C., Chen, H. M. & Hu, X. Tracking high-valent surface iron species in the oxygen evolution reaction on cobalt iron (oxy)hydroxides. *Energy Environ. Sci.* https://doi.org/10.1039/d1ee02999a (2021).
25. Loos, S., Zaharieva, I., Chernev, P., Lißner, A. & Dau, H. Electromodified NiFe alloys as electrocatalysts for water oxidation: mechanistic implications of time-resolved UV/Vis tracking of oxidation state changes. *ChemSusChem* **12**, 1966–1976 (2019).
26. Corby, S. et al. Separating bulk and surface processes in NiO_x electrocatalysts for water oxidation. *Sustain. Energy Fuels* **4**, 5024–5030 (2020).
27. Francàs, L. et al. Spectroelectrochemical study of water oxidation on nickel and iron oxyhydroxide electrocatalysts. *Nat. Commun.* **10**, 5208 (2019).
28. Risch, M. et al. Water oxidation by amorphous cobalt-based oxides: in situ tracking of redox transitions and mode of catalysis. *Energy Environ. Sci.* **8**, 661–674 (2015).
29. Song, J. et al. A review on fundamentals for designing oxygen evolution electrocatalysts. *Chem. Soc. Rev.* **49**, 2196–2214 (2020).
30. Dionigi, F. & Strasser, P. NiFe-based (oxy)hydroxide catalysts for oxygen evolution reaction in non-acidic electrolytes. *Adv. Energy Mater.* **6**, 1600621 (2016).
31. Frei, H. Time-resolved vibrational and electronic spectroscopy for understanding how charges drive metal oxide catalysts for water oxidation. *J. Phys. Chem. Lett.* **13**, 7952–7964 (2022).
32. Hu, B., Kuo, D.-Y., Paik, H., Schlom, D. G. & Suntivich, J. Enthalpy and entropy of oxygen electroadsorption on RuO_2(110) in alkaline media. *J. Chem. Phys.* **152**, 094704 (2020).
33. Kuo, D.-Y. et al. Influence of surface adsorption on the oxygen evolution reaction on IrO_2(110). *J. Am. Chem. Soc.* **139**, 3473–3479 (2017).
34. Laborda, E., García-Martínez, J. & Molina, A. Spectroelectrochemistry for the study of reversible electrode reactions with complex stoichiometries. *Electrochem. Commun.* **123**, 106915 (2021).
35. Elvers, B. J. et al. Towards operando IR- and UV–Vis-spectro-electrochemistry: a comprehensive matrix factorisation study on sensitive and transient molybdenum and tungsten mono-dithiolene complexes. *Chem. Methods* **1**, 22–35 (2021).
36. Zhai, Y., Zhu, Z., Zhou, S., Zhu, C. & Dong, S. Recent advances in spectroelectrochemistry. *Nanoscale* **10**, 3089–3111 (2018).
37. Niu, J. & Dong, S. Transmission spectroelectrochemistry. *Rev. Anal. Chem.* **15**, 1–171 (1996).
38. Goldsmith, Z. K. et al. Characterization of NiFe oxyhydroxide electrocatalysts by integrated electronic structure calculations and spectroelectrochemistry. *Proc. Natl Acad. Sci. USA* **114**, 3050–3055 (2017).
39. Boyle, W. S. & Smith, G. E. Charge coupled semiconductor devices. *Bell Syst. Tech. J.* **49**, 587–593 (1970).
40. Fossum, E. R. Active pixel sensors: are CCDs dinosaurs? *Charg. Coupled Devices Solid State Opt. Sens.* https://doi.org/10.1117/12.148585 (1993).
41. Hirayama, T. The evolution of CMOS image sensors. In 2013 *IEEE Asian Solid-State Circuits Conf.* (*A-SSCC*) 5–8 (IEEE, 2013).

42. Elgrishi, N. et al. A practical beginner's guide to cyclic voltammetry. *J. Chem. Educ.* **95**, 197–206 (2018).
43. Astuti, Y., Topoglidis, E., Gilardi, G. & Durrant, J. R. Cyclic voltammetry and voltabsorptometry studies of redox proteins immobilised on nanocrystalline tin dioxide electrodes. *Bioelectrochemistry* **63**, 55–59 (2004).
44. Zheng, W. iR compensation for electrocatalysis studies: considerations and recommendations. *ACS Energy Lett.* **8**, 1952–1958 (2023).
45. Wei, C. et al. Recommended practices and benchmark activity for hydrogen and oxygen electrocatalysis in water splitting and fuel cells. *Adv. Mater.* **31**, 1806296 (2019).
46. Stevens, M. B., Trang, C. D. M., Enman, L. J., Deng, J. & Boettcher, S. W. Reactive Fe-sites in Ni/Fe (oxy)hydroxide are responsible for exceptional oxygen electrocatalysis activity. *J. Am. Chem. Soc.* **139**, 11361–11364 (2017).
47. Conway, B. E. & Bourgault, P. L. The electrochemical behavior of the nickel–nickel oxide electrode. *Can. J. Chem.* **37**, 292–307 (1959).
48. Martinson, C. A., van Schoor, G., Uren, K. R. & Bessarabov, D. Characterisation of a PEM electrolyser using the current interrupt method. *Int. J. Hydrog. Energy* **39**, 20865–20878 (2014).
49. Watkins, N. B. et al. Resin 3D printing enables accessible electrochemical cell design. *Chem. Catal.* **4**, 101120 (2024).
50. Benck, J. D., Pinaud, B. A., Gorlin, Y. & Jaramillo, T. F. Substrate selection for fundamental studies of electrocatalysts and photoelectrodes: inert potential windows in acidic, neutral, and basic electrolyte. *PLoS ONE* **9**, e107942 (2014).
51. Rao, R. R. et al. Spectroelectrochemical analysis of the water oxidation mechanism on doped nickel oxides. *J. Am. Chem. Soc.* **144**, 7622–7633 (2022).
52. Lerner, J. M. Imaging spectrometer fundamentals for researchers in the biosciences — a tutorial. *Cytom. Part A* **69A**, 712–734 (2006).
53. Vu, P. et al. Design of prototype scientific CMOS image sensors. *High Energy Opt. Infrared Detect. Astron. III* https://doi.org/10.1117/12.790229 (2008).
54. Chen, Z., Dinh, H. N. & Miller, E. Photoelectrochemical water splitting. *Standards Exp. Methods Protoc.* https://doi.org/10.1007/978-1-4614-8298-7 (2013).
55. Lewandowski, A., Jakobczyk, P., Galinski, M. & Biegun, M. Self-discharge of electrochemical double layer capacitors. *Phys. Chem. Chem. Phys.* **15**, 8692–8699 (2013).
56. Nong, H. N. et al. Key role of chemistry versus bias in electrocatalytic oxygen evolution. *Nature* **587**, 408–413 (2020).
57. Cheng, J. et al. Brønsted–Evans–Polanyi relation of multistep reactions and volcano curve in heterogeneous catalysis. *J. Phys. Chem. C* **112**, 1308–1311 (2008).
58. Akhade, S. A., Nidzyn, R. M., Rostamikia, G. & Janik, M. J. Using Brønsted–Evans–Polanyi relations to predict electrode potential-dependent activation energies. *Catal. Today* **312**, 82–91 (2018).
59. Vojvodic, A. et al. On the behavior of Brønsted–Evans–Polanyi relations for transition metal oxides. *J. Chem. Phys.* **134**, 244509 (2011).
60. Rossmeisl, J., Qu, Z.-W., Zhu, H., Kroes, G.-J. & Nørskov, J. K. Electrolysis of water on oxide surfaces. *J. Electroanal. Chem.* **607**, 83–89 (2007).
61. Man, I. C. et al. Universality in oxygen evolution electrocatalysis on oxide surfaces. *ChemCatChem* **3**, 1159–1165 (2011).
62. Frydendal, R., Paoli, E. A., Chorkendorff, I., Rossmeisl, J. & Stephens, I. E. L. Toward an active and stable catalyst for oxygen evolution in acidic media: Ti-stabilized MnO_2. *Adv. Energy Mater.* **5**, 1500991 (2015).
63. Seh, Z. W. et al. Combining theory and experiment in electrocatalysis: insights into materials design. *Science* **355**, eaad4998 (2017).
64. Scott, S. B. et al. The low overpotential regime of acidic water oxidation part I: the importance of O_2 detection. *Energy Environ. Sci.* **15**, 1977–1987 (2022).
65. Burke, M. S., Kast, M. G., Trotochaud, L., Smith, A. M. & Boettcher, S. W. Cobalt–iron (oxy) hydroxide oxygen evolution electrocatalysts: the role of structure and composition on activity, stability, and mechanism. *J. Am. Chem. Soc.* **137**, 3638–3648 (2015).
66. Aggarwal, S. et al. PyTASER: simulating transient absorption spectroscopy (TAS) for crystals from first principles. *J. Open Source Softw.* **9**, 5999 (2024).
67. Guevarra, D. et al. Orchestrating nimble experiments across interconnected labs. *Digit. Discov.* **2**, 1806–1812 (2023).

Acknowledgements
B.M. acknowledges the Lindemann Trust and Schmidt Sciences for funding. He is also indebted to K. K. Lim and X. Li for thoughtful discussion that clarified many points on this work. J.R.D. and I.E.L.S. acknowledge the BP International Centre for Advanced Materials (bp-ICAM) as well as the EPSRC grant EP/W033232/1, which made this research possible. This project was supported by the Royal Academy of Engineering under the Research Fellowship programme (R.R.R.). C.L. acknowledges the Imperial College London and China Scholarship Council for the IC–CSC joint scholarship.

Author contributions
Introduction: B.M., C.L., L.G.V., S.S., R.R.R., I.E.L.S. and J.R.D.; Experimentation: B.M., C.L., A.C., L.G.V., S.S., K.M., R.R.R., I.E.L.S. and J.R.D.; Results: B.M., C.L., A.C., S.S., K.M., A.W., R.R.R., I.E.L.S., J.R.D. and R.J.R.J.; Applications: B.M., C.L., A.C., S.S., K.M., R.R.R., I.E.L.S. and J.R.D.; Reproducibility and data deposition: B.M., C.L., S.S., R.R.R., I.E.L.S. and J.R.D.; Limitations and optimizations: B.M., C.L., A.C., L.G.V., S.S., K.M., A.W., R.R.R., I.E.L.S. and J.R.D.; Outlook: B.M., C.L., A.C., L.G.V., S.S., R.R.R., I.E.L.S. and J.R.D.

Competing interests
A.C. is an employee of Oxford Instruments Andor (OIA) and contributed his perspective to discussions of the detector technologies with respect to the SEC spectroscopic methodology. No financial or commercial support has been provided by OIA. All other authors declare no competing interests.

Additional information
Supplementary information The online version contains supplementary material available at https://doi.org/10.1038/s43586-025-00445-4.

Peer review information *Nature Reviews Methods Primers* thanks Evgenia Dmitrieva, Marcel Risch and the other, anonymous, reviewer(s) for their contribution to the peer review of this work.

Related links
GitHub archive: https://github.com/BenjaminSMoss/NRMP
ixdat: https://ixdat.readthedocs.io